



MINISTÉRIO DA CIÊNCIA, TECNOLOGIA, INOVAÇÕES E COMUNICAÇÕES
INSTITUTO NACIONAL DE PESQUISAS ESPACIAIS

sid.inpe.br/mtc-m21c/2018/07.23.04.02-TDI

**GENERATION AND PROPAGATION OF MSTIDS
EXCITED BY AURORAL HEATING: OBSERVATIONS
AND SIMULATIONS**

Ricardo da Rosa Paes

Doctorate Thesis of the Graduate Course in Spatial Geophysics/Solar and Terrestrial Environment Sciences, guided by Drs. Esfhan Alam Kherani, and Inez Staciarini Batista, approved in May 29, 2018.

URL of the original document:

<<http://urlib.net/8JMKD3MGP3W34R/3RGC3AP>>

INPE
São José dos Campos
2018

PUBLISHED BY:

Instituto Nacional de Pesquisas Espaciais - INPE

Gabinete do Diretor (GBDIR)

Serviço de Informação e Documentação (SESID)

CEP 12.227-010

São José dos Campos - SP - Brasil

Tel.:(012) 3208-6923/7348

E-mail: pubtc@inpe.br

**COMMISSION OF BOARD OF PUBLISHING AND PRESERVATION
OF INPE INTELLECTUAL PRODUCTION (DE/DIR-544):****Chairperson:**

Dr. Marley Cavalcante de Lima Moscati - Centro de Previsão de Tempo e Estudos Climáticos (CGCPT)

Members:

Dra. Carina Barros Mello - Coordenação de Laboratórios Associados (COCTE)

Dr. Alisson Dal Lago - Coordenação-Geral de Ciências Espaciais e Atmosféricas (CGCEA)

Dr. Evandro Albiach Branco - Centro de Ciência do Sistema Terrestre (COCST)

Dr. Evandro Marconi Rocco - Coordenação-Geral de Engenharia e Tecnologia Espacial (CGETE)

Dr. Hermann Johann Heinrich Kux - Coordenação-Geral de Observação da Terra (CGOBT)

Dra. Ieda Del Arco Sanches - Conselho de Pós-Graduação - (CPG)

Silvia Castro Marcelino - Serviço de Informação e Documentação (SESID)

DIGITAL LIBRARY:

Dr. Gerald Jean Francis Banon

Clayton Martins Pereira - Serviço de Informação e Documentação (SESID)

DOCUMENT REVIEW:

Simone Angélica Del Ducca Barbedo - Serviço de Informação e Documentação (SESID)

André Luis Dias Fernandes - Serviço de Informação e Documentação (SESID)

ELECTRONIC EDITING:

Marcelo de Castro Pazos - Serviço de Informação e Documentação (SESID)

Murilo Luiz Silva Gino - Serviço de Informação e Documentação (SESID)



MINISTÉRIO DA CIÊNCIA, TECNOLOGIA, INOVAÇÕES E COMUNICAÇÕES
INSTITUTO NACIONAL DE PESQUISAS ESPACIAIS

sid.inpe.br/mtc-m21c/2018/07.23.04.02-TDI

**GENERATION AND PROPAGATION OF MSTIDS
EXCITED BY AURORAL HEATING: OBSERVATIONS
AND SIMULATIONS**

Ricardo da Rosa Paes

Doctorate Thesis of the Graduate Course in Spatial Geophysics/Solar and Terrestrial Environment Sciences, guided by Drs. Esfhan Alam Kherani, and Inez Staciarini Batista, approved in May 29, 2018.

URL of the original document:

<<http://urlib.net/8JMKD3MGP3W34R/3RGC3AP>>

INPE
São José dos Campos
2018

Cataloging in Publication Data

Paes, Ricardo da Rosa.

P138g Generation and propagation of MSTIDs excited by auroral heating: observations and simulations / Ricardo da Rosa Paes. – São José dos Campos : INPE, 2018.
xvi + 58 p. ; (sid.inpe.br/mtc-m21c/2018/07.23.04.02-TDI)

Thesis (Doctorate in Geophysics/Solar and Terrestrial Environment Sciences) – Instituto Nacional de Pesquisas Espaciais, São José dos Campos, 2018.

Guiding : Drs. Esfhan Alam Kherani, and Inez Staciari Batista.

1. Acoustic-gravity waves. 2. MSTID. 3. Auroral heating. 4. Numerical simulation. 5. Polar ionosphere. I.Title.

CDU 551.510.535



Esta obra foi licenciada sob uma Licença [Creative Commons Atribuição-NãoComercial 3.0 Não Adaptada](https://creativecommons.org/licenses/by-nc/3.0/).

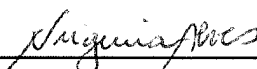
This work is licensed under a [Creative Commons Attribution-NonCommercial 3.0 Unported License](https://creativecommons.org/licenses/by-nc/3.0/).

Aluno (a): *Ricardo da Rosa Paes*

Título: "GENERATION AND PROPAGATION OF MSTIDs EXCITED BY AURORAL HEATING: OBSERVATIONS AND SIMULATIONS".

Aprovado (a) pela Banca Examinadora
em cumprimento ao requisito exigido para
obtenção do Título de *Doutor(a)* em
*Geofísica Espacial/Ciências do Ambiente
Solar-Terrestre*

Dra. Maria Virginia Alves

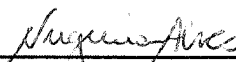


Presidente / INPE / SJC Campos - SP

Participação por Video - Conferência

Aprovado Reprovado

Dr. Esfhan Alam Kherani

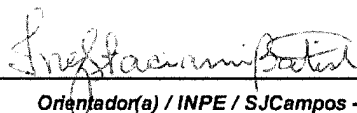


Orientador(a) / INPE / SJC Campos - SP

Participação por Video - Conferência

Aprovado Reprovado

Dra. Inez Staciariini Batista



Orientador(a) / INPE / SJC Campos - SP

Participação por Video - Conferência

Aprovado Reprovado

Dr. Hisao Takahashi




Membro da Banca / INPE / SJC Campos - SP

Participação por Video - Conferência

Aprovado Reprovado

Dra. Cláudia Maria Nicoli Cândido



Membro da Banca / INPE / São José dos Campos - SP

Participação por Video - Conferência

Aprovado Reprovado

Este trabalho foi aprovado por:

maioria simples

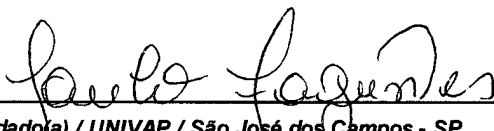
unanimidade

São José dos Campos, 29 de maio de 2018

Aprovado (a) pela Banca Examinadora
em cumprimento ao requisito exigido para
obtenção do Título de **Doutor(a)** em

**Geofísica Espacial/Ciências do Ambiente
Solar-Terrestre**

Dr. Paulo Roberto Fagundes

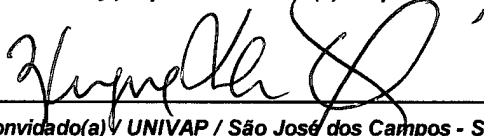


Convidado(a) / UNIVAP / São José dos Campos - SP

Participação por Video - Conferência

Aprovado Reprovado

Dra. Virginia Klausner de Oliveira



Convidado(a) / UNIVAP / São José dos Campos - SP

Participação por Video - Conferência

Aprovado Reprovado

Este trabalho foi aprovado por:

maioria simples

unanimidade

ACKNOWLEDGEMENTS

Meus mais sinceros agradecimentos ao Dr. Esfhan Alam Kherani e Dra. Inez Staciariini Batista pela orientação neste trabalho.

Agradeço também à Coordenação de Aperfeiçoamento de Pessoal de Nível Superior (CAPES) que concedeu uma bolsa complementar nos primeiros anos de doutoramento e ao Conselho Nacional de Desenvolvimento Científico e Tecnológico que concedeu uma bolsa para os anos finais desta tese de doutorado. Agradeço ao Conselho de Pós-Graduação do curso de Geofísica Espacial do INPE pela disponibilização de recursos que complementaram a realização deste trabalho.

ABSTRACT

In this work, we present a numerical simulation study of the acoustic-gravity waves. We developed a simulation model that solves the Navier-Stokes hydrodynamic equations in the atmosphere covering 0-600 km altitudes and 70° - 0° geographic latitudes in both hemispheres. Using these equations, we derive the wave equation for the AGWs which contains the terms of acoustic wave, gravity wave, viscous dissipation and source. The source terms may be chosen in the form of the temperature (auroral heating) or the density fluctuations (precipitation) in the auroral region. We consider these fluctuations to be of Gaussian form in space centered between 100 and 120 km altitude, with the amplitude equals to 1% of the ambient. The model was applied to study the propagation characteristics of MSTIDs in the polar ionosphere on December 8, 2009 (dayside). The same MSTID was identified on a previous study using an all-sky imager in the Norwegian ionosphere. This MSTID was found to propagate equator-eastward with the average velocity of ~ 60 -100 m/s and their wavefronts were aligned in Southwest-Northeast direction. Some characteristics identified in our observations suggest that the horizontal coverage of AGWs is proportional to the horizontal Gaussian spread of the Joule heating source. It also implies that this source is capable of launching AGW which propagates long distance in latitude without much attenuation.

Keywords: Acoustic-gravity waves. MSTID. Auroral heating. Numerical simulation. Polar ionosphere.

GERAÇÃO E PROPAGAÇÃO DE MSTIDS EXCITADAS POR AQUECIMENTO AURORAL: OBSERVAÇÕES E SIMULAÇÕES

RESUMO

Neste trabalho é apresentado um estudo de simulação numérica das ondas de gravidade acústica. Para isso, foi desenvolvido um modelo de simulação que resolve as equações hidrodinâmicas de Navier-Stokes na atmosfera capaz de cobrir um intervalo de 0-600 km de altitude e 70° - 0° de latitude geográfica em ambos os hemisférios. A partir de tais equações foi possível deduzir a equação de onda para as AGWs onde os termos de onda acústica, onda gravitacional, dissipação por viscosidade e para fonte. Os termos da fonte podem ser estabelecidos na forma de flutuações de temperatura (aquecimento auroral) ou de densidade de partículas (precipitação) na região auroral. Neste modelo foi considerado que estas flutuações possuem a forma Gaussiana em um espaço centrado ente 100 e 120 km de altitude, com a amplitude equivalente a 1% do ambiente. O modelo foi aplicado para estudar as características de propagação de MSTIDs na ionosfera polar no lado diurno no dia 8 de dezembro de 2009. O mesmo MSTID foi identificado em um estudo anterior através de um imageador all-sky na ionosfera norueguesa. Este MSTID propagava-se na direção equador-leste com a velocidade média de ~ 60 - 100 m/s, com suas frentes de onda alinhadas na direção Sudoeste-Nordeste. Algumas características identificadas nas observações desta tese sugerem que a cobertura horizontal dos AGWs é proporcional à propagação Gaussiana horizontal da fonte de aquecimento Joule. Isso também implica que essa fonte é capaz de lançar AGWs que se propagam a longas distâncias em termos de latitude sem muita atenuação.

Palavras-chave: Ondas de gravidade acústica. MSTID. Aquecimento auroral. Simulação numérica. Ionosfera polar.

LIST OF FIGURES

	<u>Page</u>
1.1 Daytime altitude variations of Number densities of various Atmospheric and Ionospheric constituents.	1
1.2 Radio wave dispersion in the Ionosphere.	2
1.3 Schematic of Magnetosphere-Ionosphere system.	5
1.4 Polar ionosphere: Polar cap is the region dominated by the IMF electric field directly mapped from solar wind by field-aligned Birkeland current.	6
1.5 TIDs in the form of Total-Electron-Content (TEC) disturbance as measured from GNSS receivers at mid-high latitudes.	9
1.6 TIDs in the polar Ionosphere: Airglow disturbances as observed from all-sky imager over Norway. Their presence is an indication of atmospheric and ionospheric disturbances since airglow is result of chemical reactions involving atmosphere and ionosphere.	10
2.1 CHAIN receivers (denoted by stars) on 2009 and corresponding IPP trajectories projected at 300 km altitude.	12
2.2 Adjustments for the horizontal (top) and the phase (bottom) keograms theoretical profiles.	14
3.1 TEC measurements from the station Cambridge Bay located at $68.97^{\circ}N$: (Upper panel) The gray curves and the superimposed red curve represents TEC from each PRN and the average TEC over all PRN respectively (Lower panel): The wavelet spectra of TEC is shown. The rectangle frame covers the time zone of interest.	24
3.2 The latitude keograms for 4 frequency bands, 15-25, 35-45, 55-65 and 75-85 minutes, respectively.	25
3.3 (a-b) Latitude and longitude keograms constructed by considering the IPP trajectories of PRNs=10,16. (c-d) Latitude and longitude keograms constructed by considering the IPP trajectories of all PRNs. In the latitude and longitude keograms, two green lines with different slopes (as denoted by numbers in green colors) are drawn. Also drawn are the black lines along which phases are aligned i.e. they are few identified wavefronts.	26
3.4 Snapshots of Δ TEC at four chosen times, as mentioned at the top of each panel. These maps are constructed by 4 point interpolation of original IPP points. In each panel, a green line is drawn along which wavefronts are aligned and successively distancing away equator-eastward.	27

3.5	(a) Magnetic field disturbances Δb_z obtained by de-trending the vertical magnetic field component measured from CANMOS magnetometer network are shown. (b) Δb_z (blue curve) at Cambridge Bay and ΔTEC^2 (red curves) at three stations surrounding Cambridge Bay are shown.	28
4.1	CHAIN from 2015 onwards. The black stars represent receivers of CHAIN network before 2015.	34
4.2	Seasonal Variabilities on year 2016: Latitude keograms of ΔTEC on winter and summer 2016. The black squares indicate the sunrise time and the red circles indicate the sunset time	35
4.3	Seasonal Variabilities on year 2016: Latitude keograms of ΔTEC on spring and winter equinoxes 2016. The black squares indicate the sunrise time and the red circles indicate the sunset time.	36
4.4	Latitude keograms of ΔTEC on winter/summer on low-solar flux year 2017. The black squares indicate the sunrise time and the red circles indicate the sunset time.	37
4.5	Latitude keograms of ΔTEC on winter/summer on high solar flux year 2014. The black squares indicate the sunrise time and the red circles indicate the sunset time.	38
4.6	Spectrogram of TEC data derived from receiver at CambridgeBay (CBB) on year 2013. The TEC data on representative days of 12 months are plotted in panels and the number of day is denoted at the top of each panel.	39
4.7	Spectrogram of TEC data derived from receiver at CambridgeBay (CBB) on year 2014. The TEC data on representative days of 12 months are plotted in panels and the number of day is denoted at the top of each panel.	40
4.8	Spectrogram of TEC data derived from receiver at CambridgeBay (CBB) on year 2015. The TEC data on representative days of 12 months are plotted in panels and the number of day is denoted at the top of each panel. The unusal spectrogram on day 288 is not physical and is caused by unavailability of data.	41
4.9	Spectrogram of TEC data derived from receiver at CambridgeBay (CBB) on year 2016. The TEC data on representative days of 12 months are plotted in panels and the number of day is denoted at the top of each panel.	42

5.1	Geomagnetic Disturbances (GMDs) observations: Spectrogram of magnetic field data derived from magnetometer at Cambridge Bay (CBB) on year 2013. The magnetic data on representative days of 12 months are plotted in panels and the number of day is denoted at the top of each panel.	46
5.2	Geomagnetic Disturbances (GMDs) observations: Spectrogram of magnetic field data derived from magnetometer at Cambridge Bay (CBB) on year 2014. The magnetic data on representative days of 12 months are plotted in panels and the number of day is denoted at the top of each panel.	47
5.3	Geomagnetic Disturbances (GMDs) observations: Spectrogram of magnetic field data derived from magnetometer at Cambridge Bay (CBB) on year 2015. The magnetic data on representative days of 12 months are plotted in panels and the number of day is denoted at the top of each panel.	48
5.4	Geomagnetic Disturbances (GMDs) observations: Spectrogram of magnetic field data derived from magnetometer at Cambridge Bay (CBB) on year 2016. The magnetic data on representative days of 12 months are plotted in panels and the number of day is denoted at the top of each panel.	49
5.5	Numerical Experiment of AGWs: The longitudinal wind component of AGWs is shown. Red and blue surfaces correspond to the positive and negative signs of the wind component. The Joule heating is centred at 105 km altitude with Gaussian spread of 20 km. It is centred at latitude-longitude of CBB and has Gaussian spread of 5° in latitude-longitude. . .	50
5.6	Numerical Experiment of AGWs: The longitudinal wind component of AGWs is shown. Red and blue surfaces correspond to the positive and negative signs of the wind component. The Joule heating is centred at 105 km altitude with Gaussian spread of 20 km. It is centred at latitude-longitude of CBB and has Gaussian spread of 5° in latitude-longitude. . .	51

CONTENTS

	<u>Page</u>
1 INTRODUCTION	1
1.1 Geosphere	1
1.2 Ionospheric currents and electric field	3
1.3 Polar Ionosphere	4
1.4 Traveling Ionospheric Disturbances	7
1.5 Objectives of the present thesis	7
2 AVAILABLE AND REQUIRED TOOLS	11
2.1 Measurements and Data processing	11
2.1.1 CHAIN network	11
2.1.2 TEC measurements	12
2.1.3 Keogram method	13
2.2 Numerical Experiments of MSTIDs	13
2.2.1 Joule heating associated with the auroral precipitation dynamics	16
3 MSTIDS ON DAY 08 OF DECEMBER 2009	19
3.1 CHAIN network and data analysis	19
3.2 Results and Discussion	20
3.3 Summary	22
4 SEASONAL AND SOLAR-FLUX VARIABILITIES OF MSTIDS 29	
4.1 Results and Discussion	29
4.1.1 Seasonal variability	30
4.1.2 Solar-flux variability	30
4.1.3 Seasonal and solar-flux variabilities of Spectral characteristics	32
4.2 Summary	33
5 POSSIBLE ORIGIN MECHANISMS OF MSTIDS	43
5.1 Quiet-time Geomagnetic Disturbances (GMDs) in the polar cap/oval re- gion	43
5.2 Numerical Experiments	44
6 CONCLUSIONS	53

REFERENCES 55

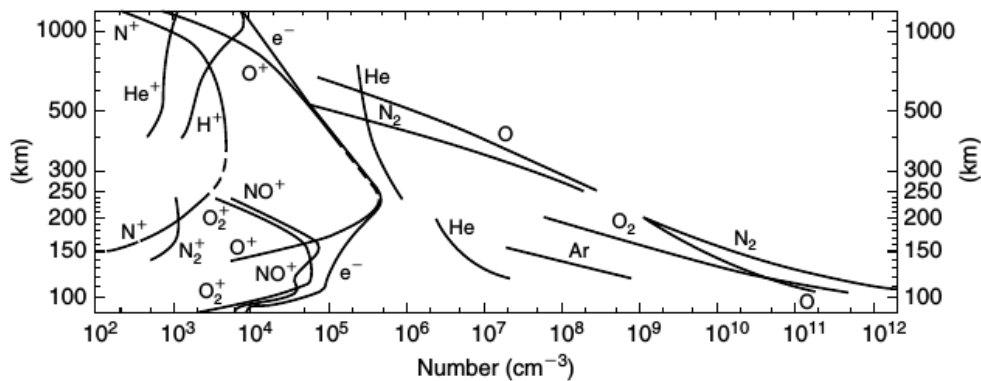
1 INTRODUCTION

1.1 Geosphere

Space around Earth's surface is known as the Geosphere that directly influences the terrestrial life. An important member of the Geosphere is the Atmosphere that is located in the altitude range of 0-1000 km and made up of neutrals essential for sustainable nature (PROLSS, 2004; KELLEY, 2009).

Above 60 km altitude, the solar photons in the EUV energy range ionize the atmosphere and as a consequence, a partially ionized plasma called Ionosphere, is formed. The ionosphere is organized in layers, namely, D (60-80 km), E (80-130 km) and F (130-1000 km) layers. The ionosphere is coupled with the atmosphere through collisions and this coupling is characterized by collision frequency ($\nu_{\alpha n}$). It is also coupled with the geomagnetic field characterized by gyrofrequency (Ω_{α}). Here α is the ionospheric plasma fluids. The D,E and F layers are classified based on competing role of $\nu_{\alpha n}$ and Ω_{α} . In the D region, both ions and electrons are controlled by neutrals while in the F region, both are controlled by the geomagnetic field. In the E region, the ions are controlled by geomagnetic field while electrons are controlled by neutrals (PROLSS, 2004). Figure 1.1 shows the vertical distribution of the most significant ions and neutral elements.

Figure 1.1 - Daytime altitude variations of Number densities of various Atmospheric and Ionospheric constituents.



SOURCE: Kelley (2009)

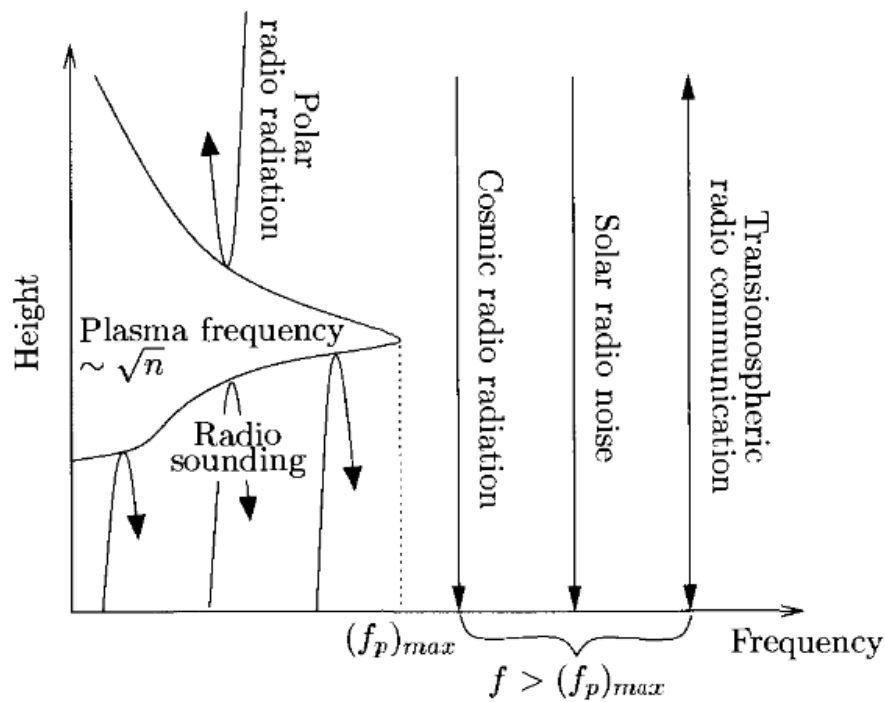
The ionospheric plasma is characterized by the plasma frequency given as follows:

$$\omega_p = \left(\frac{q^2}{\epsilon_0 m_e} n \right)^{1/2} \quad (1.1)$$

Here (n) is the ionospheric electron density. For typical range $10^9 \leq n \leq 10^{12} \text{ m}^{-3}$, ω_p occupies 1-20 MHz i.e. the HF radio frequency range. Therefore, the ionosphere interacts efficiently with radio waves and behaves as dispersive medium.

On this basis, the radio sounding of ionosphere is the most employed diagnostic tool. The ionosonde, incoherent and coherent backscatter radar and GNSS radio sounding satellites are noteworthy probes to monitor the ionospheric dynamics. Figure 1.2 shows a schematic of the various frequencies used in ionospheric research.

Figure 1.2 - Radio wave dispersion in the Ionosphere.



SOURCE: Prolss (2004)

1.2 Ionospheric currents and electric field

Atmospheric motion i.e. the neutral wind (W) is the primarily forcing, responsible for the ionospheric currents. However, this current is not divergence-free due to the spatial varying electron density and W . As a result, an electric field (E) is developed to drive the dynamo current (J_d) so that the total current becomes divergence-free. Mathematically, it is described as follows:

The ionospheric motion and current (U_α, J_w) due to W is given by following expressions (KELLEY, 2009):

$$U_\alpha = \mu_p(W \times B_o) + \mu_h(W \times B_o) \times b + \mu_o W \cdot B_o \quad (1.2)$$

$$J_w = \sigma_p(W \times B_o) + \sigma_h(W \times B_o) \times b + \sigma_o W \cdot B_o \quad (1.3)$$

where (μ_p, μ_h, μ_o) are the Pederson, Hall and parallel mobilities and ($\sigma_p, \sigma_h, \sigma_o$) are the Pederson, Hall and parallel conductivities. In general, the relation between μ given as follows:

$$\sigma = \sum n_\alpha q_\alpha \mu_\alpha = ne(\mu_i - \mu_e) \quad (1.4)$$

In general,

$$\nabla \cdot J_w \neq 0 \quad (1.5)$$

and therefore, the dynamo electric field (E) drives dynamo current (J_d), given by following expression:

$$J_d = \sigma_p E + \sigma_h E \times b + \sigma_o E_{||} \quad (1.6)$$

so that the total current is divergence-free i.e.,

$$\nabla \cdot (J_w + J_d) = 0 \Rightarrow \nabla \cdot (\bar{\sigma} \cdot E) = \nabla \cdot J_w \quad (1.7)$$

In essence, the neutral wind is the source of the ionospheric electric field. The total ionospheric velocity is given as follows:

$$U_\alpha = \mu_p(E + W \times B_o) + \mu_h(E + W \times B_o) \times b + \mu_o(E \cdot b + W \cdot B_o) \quad (1.8)$$

This motion is responsible for the number density change, governed by the continuity equation, as follows:

$$\frac{\partial n}{\partial t} + \nabla \cdot (n U_\alpha) = P + L \quad (1.9)$$

In general, the E and F region are respectively, current (motor) and electric field (load) in the ionospheric circuit and they are connected through the highly con-

ducting equi-potential geomagnetic field lines. The circuit is closed through zonally separated field lines in the E region.

The neutral wind (W) arises from varieties of forcing and almost all of them are associated with solar heating and gravitational forcing. In general, these forcings are counterbalanced by the Earth's gravitational force associated buoyancy, resulting into the large scale Atmospheric waves, commonly known as Tides.

Apart from the large scale solar forcing, localized small scale solar forcing arises due to the geographical inhomogeneity and this leads to the small scale atmospheric waves, known as the Acoustic-Gravity waves (AGWs).

Both Tides and AGWs are predominantly upward propagating waves since the solar forcing increases with decreasing altitude. An interesting aspect of these waves is that their amplitudes are inversely proportional to the atmospheric density and therefore it increases exponentially with altitude and can be amplified by 3-4 order while propagating from lower atmosphere to upper atmosphere. This characteristic makes these buoyancy waves as dominant waves in the thermosphere where they dissipate owing to the viscosity. Since the ionosphere is collocated within the thermosphere, the neutral wind associated with these buoyancy waves are dominant forcing for the dynamo currents and electric field, as discussed in the last section.

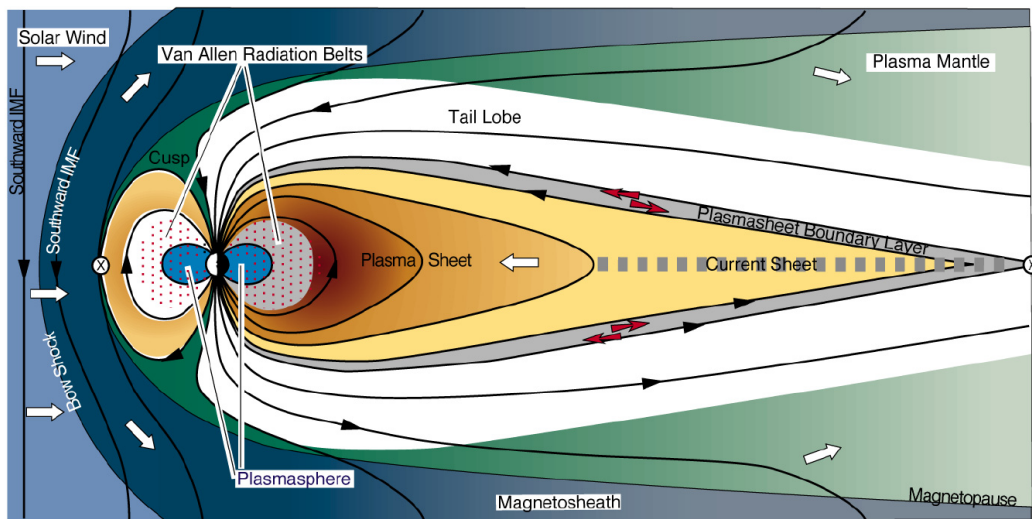
The Tides are responsible for the large scale electric field which is responsible for diurnal and semi-diurnal variations in the ionosphere. The tides are largely dissipated in the lower thermosphere that hosts ionospheric E region.

1.3 Polar Ionosphere

The polar ionosphere i.e., the high-latitude ionosphere is located in geomagnetic latitude $> \pm 50^\circ$ in both Northern and Southern hemisphere. Owing to its connection to the magnetosphere as shown in Figure 1.3, it presents scenario which is different from the mid-latitude ($25^\circ - 50^\circ$) and low-latitude ($0^\circ - 25^\circ$) Ionosphere.

The polar ionosphere is subdivided into three regions: Polar cap in $\pm(90^\circ - 70^\circ)$, polar oval in $\pm(70^\circ - 60^\circ)$ and subpolar in $< \pm 60^\circ$. The polar cap region has geomagnetic field lines extended outside the Magnetosphere and they become closed by joining to the Interplanetary Magnetic Field lines. The polar oval has geomagnetic field lines closed within the Magnetosphere. They have dipole morphology that is distorted by

Figure 1.3 - Schematic of Magnetosphere-Ionosphere system.



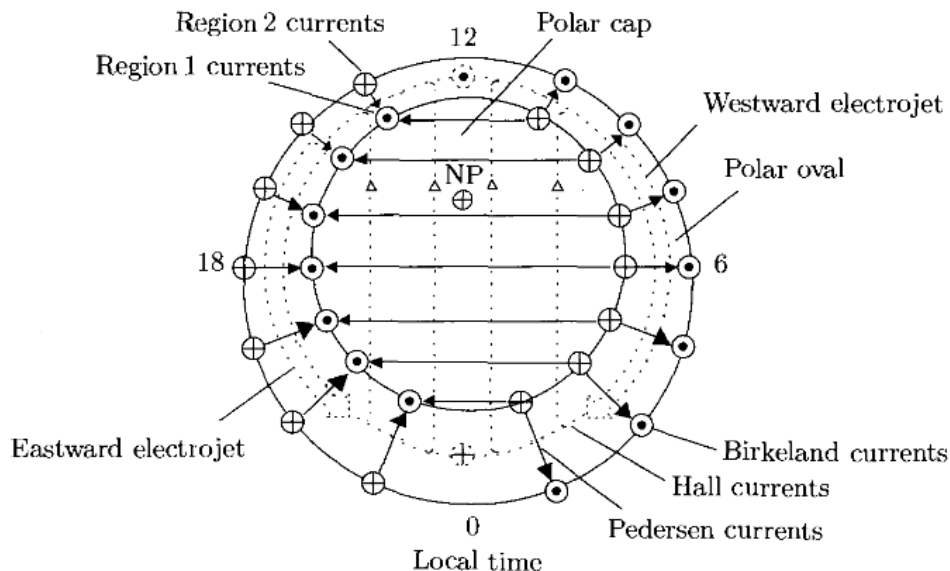
SOURCE: Hunsucker and Hargreaves (2003)

the solar wind such that on dayside (nightside) they are compressed (extended) in the direction of solar wind. The sub-polar region preserves the dipole morphology with very little effects of solar wind.

Polar oval is the most active region since the associated geomagnetic field lines have null or X points in both day and night sides. At these null points, strong plasma current sheets are formed that hosts varieties of plasma waves and instabilities. These waves accelerate the low energy ($\sim eV$) solar wind to high energy $\sim keV$ that eventually precipitates into the polar oval. Moreover, the polar oval offers strongest divergence in the current density since it is thinnest in size. As a result, strongest electric field upto about ~ 30 mV/m is developed during quiet solar conditions. Since the polar oval is sandwiched between polar cap and sub-polar regions, the wave activities, precipitations and strongest electric field within it have robust impacts on regions of both sides. These processes are manifested in the form of PC1-5 fluctuations, discrete and diffuse auroras, polar patches and Traveling Ionospheric Disturbances (TIDs), as observed from magnetometers, radars and all-sky imagers.

Mesoscale structures in the polar ionosphere consist mainly of polar patches and aurora which have a broad range of generation mechanisms and source regions. Polar cap patches form around noon near polar cusp and subsequently follow the prevailing plasma convection through the polar cap. These patches originate from higher

Figure 1.4 - Polar ionosphere: Polar cap is the region dominated by the IMF electric field directly mapped from solar wind by field-aligned Birkeland current.



SOURCE: Prolss (2004)

density plasma at LLBL (Low-Latitude Boundary Layer) and/or due to the precipitation dynamics from the cusp region. Their magnitude, spatial/temporal scales can be quite random, typically resulting in lower frequency (< 2 mHz) variations in $\Delta \text{TEC} \sim 10\text{-}15$ TECU.

Auroral forms observed in the polar ionosphere are often interpreted as footprints of electrodynamic processes in the magnetospheric boundary layer or plasma sheet boundary layer. Poleward Moving Auroral Forms (PMAFs) are midday auroral intensifications that either originate in the polar oval and are convected into the polar cap, or are as result of solar wind plasma entering the magnetosphere via boundary layers. Poleward Moving Sun-Aligned Arcs (PMSAAs) are quasi periodic variations in ΔTEC originated adjacent to the auroral oval and propagating poleward, with magnitude $\sim 1\text{-}4$ TECU and discrete frequency components in the range of 1.6-22.8 mHz. These frequencies were associated with poleward motion of the arcs and small-scale structuring within the arcs (JAYACHANDRAN et al., 2009b). Pulsating aurora in the polar ionosphere has frequency in 1-4 mHz with similar frequency pulsation in ground magnetometer data are manifestation of modulation of the precipitation by Pc5 MHD waves of magnetospheric origin (WEATHERWAX et al., 1997).

1.4 Traveling Ionospheric Disturbances

Traveling Ionospheric Disturbances (TIDs) are wavelike perturbations in the F region Ionospheric density and electric field that propagate with horizontal wavelengths of 10m-1000 km and periods of 2 minutes to 2 hours (HINES, 1974; HUNSUCKER; HARGREAVES, 2003). They are classified into three kinds: Macro, Meso and Micro scale TIDs, based on their wavelengths and periods. Among them, Mesoscale TIDs (MSTIDs) are most prominent in nature that have wavelengths in 100-1000 km and periods in 20-60 minutes (HARGREAVES, 1992). They are the manifestation of Atmosphere-Ionosphere coupling involving Atmospheric and ionospheric plasma waves (HINES, 1974). They are associated with tropospheric convections, windy climates, magnetospheric plasma precipitations in the polar ionosphere, polar vortex and so on (HARGREAVES, 1992). They propagate long distance from their origin and therefore they offer efficient way of transferring energy in space. Their presence often trigger plasma instabilities, leading to the violent highly energetic phenomena known as spread F (HUNSUCKER; HARGREAVES, 2003).

Their presence in the Ionosphere significantly alters the radio wave propagation and poses serious threat to the communication and navigation systems. For this reason, they have been the principal focus of ionospheric research during last 5 decades (HUNSUCKER; HARGREAVES, 2003). Figure 1.5 shows an example of a TID seen in TEC data (OTSUKA *et al.*, 2013).

1.5 Objectives of the present thesis

MSTIDs have been detected at various latitudes of which the high-latitude MSTIDs is of particular interest . Since high latitude is exposed to the solar wind-magnetospheric coupled dynamics, the sources that trigger MSTIDs, are plenty in the high latitude, in comparison to other latitudes (WATSON *et al.*, 2016). The high-latitude MSTIDs are observed during both geomagnetically quiet and disturbed periods. Their activity peaks in the fall and winter and minimizes in the summer. During quiet-time which is the focus of the present study, they surge during auroral intensification and/or during lower atmospheric disturbances such as the polar vortex and tropospheric convection in the polar ionosphere (HUANG *et al.*, 1998; SOFKO; HUANG, 2000; SHIOKAWA *et al.*, 2012; FRISSELL *et al.*, 2016). Based on these find-

ings, they are argued as owing to the dynamics driven by atmospheric waves and ionospheric currents. Majority of them are found to propagate equatorward that suggests them to be generated somewhere in the poleward region (HALL et al., 1999).

Although the generation mechanisms of high-latitude MSTIDs is fairly well understood observationally, these mechanisms remain partially unattained theoretically. Also their propagation characteristics remain unexplored, both experimentally/theoretically. Moreover, they are largely studied using Super-DARN HF radars (MACDOUGALL et al., 2000; ISHIDA et al., 2008; FRISSELL et al., 2016) and sometime using the all-sky imagers (SHIOKAWA et al., 2012) having capacity of scanning the ionosphere. Figure 1.6 shows a TID propagation as seen from all-sky imager (SHIOKAWA et al., 2012).

In this context, owing to its global coverage capability, the network of GNSS receivers can offer an alternative way to scan the ionosphere and to study the propagation characteristics of MSTIDs. Based on Total Electron Content (TEC) measurements from the network of GNSS receivers, numerous studies of MSTIDs are carried out in the mid-latitudes (JONAH et al., 2016). On the other hand, in the high-latitudes, such studies are few mainly due to the lack of effective GNSS network (MOSERT et al., 2011; MAKAREVICH; NICOLLS, 2013; OINATS et al., 2016).

Based on these assessments, I set up following objectives for my thesis:

1. Investigating the propagation characteristics of high-latitude MSTIDs from TEC measurements under geomagnetically quiet conditions,
2. Focusing on generation mechanism of observed MSTIDs based on numerical simulation experiments that can eventually simulate the observed propagation characteristics.

Figure 1.5 - TIDs in the form of Total-Electron-Content (TEC) disturbance as measured from GNSS receivers at mid-high latitudes.

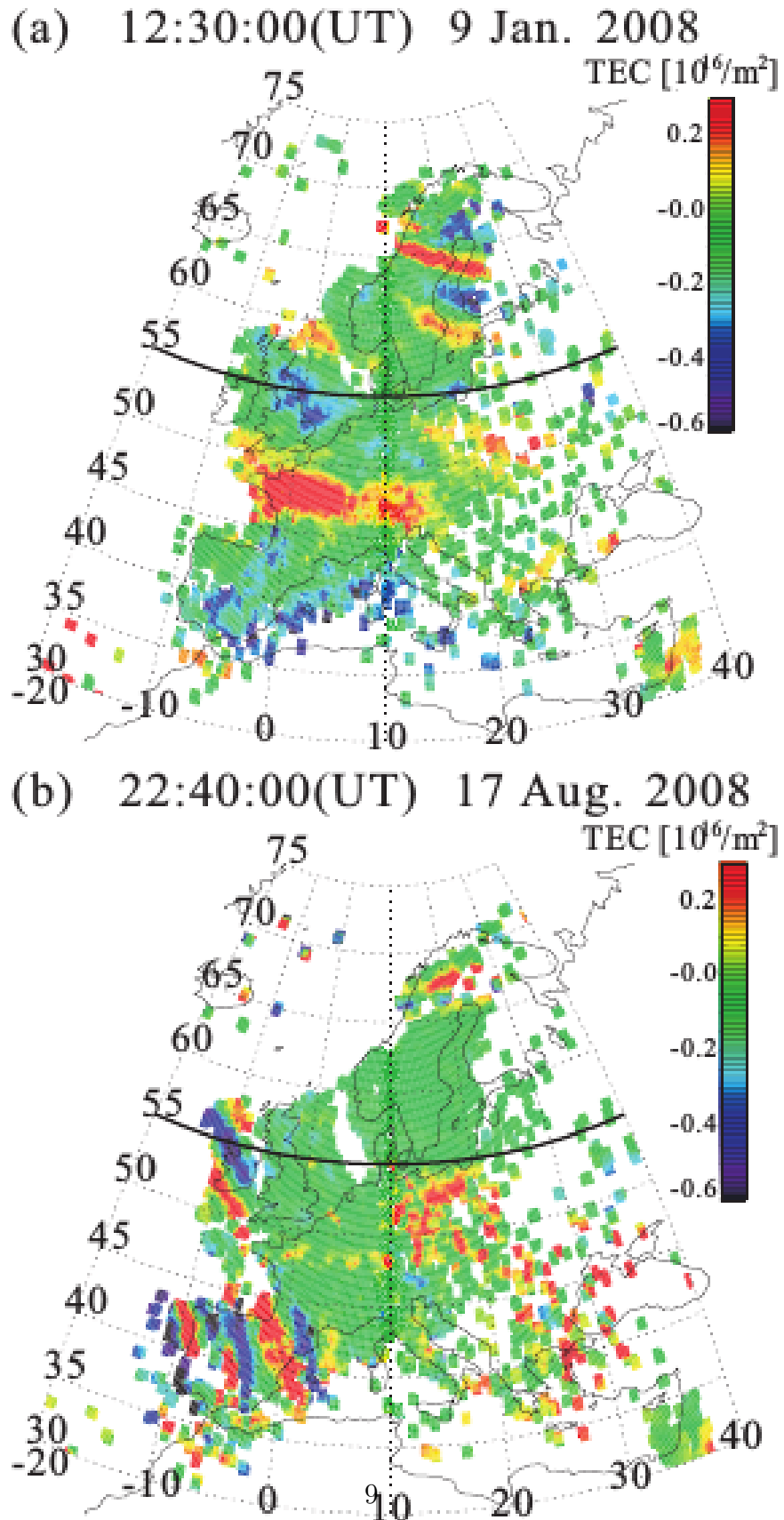
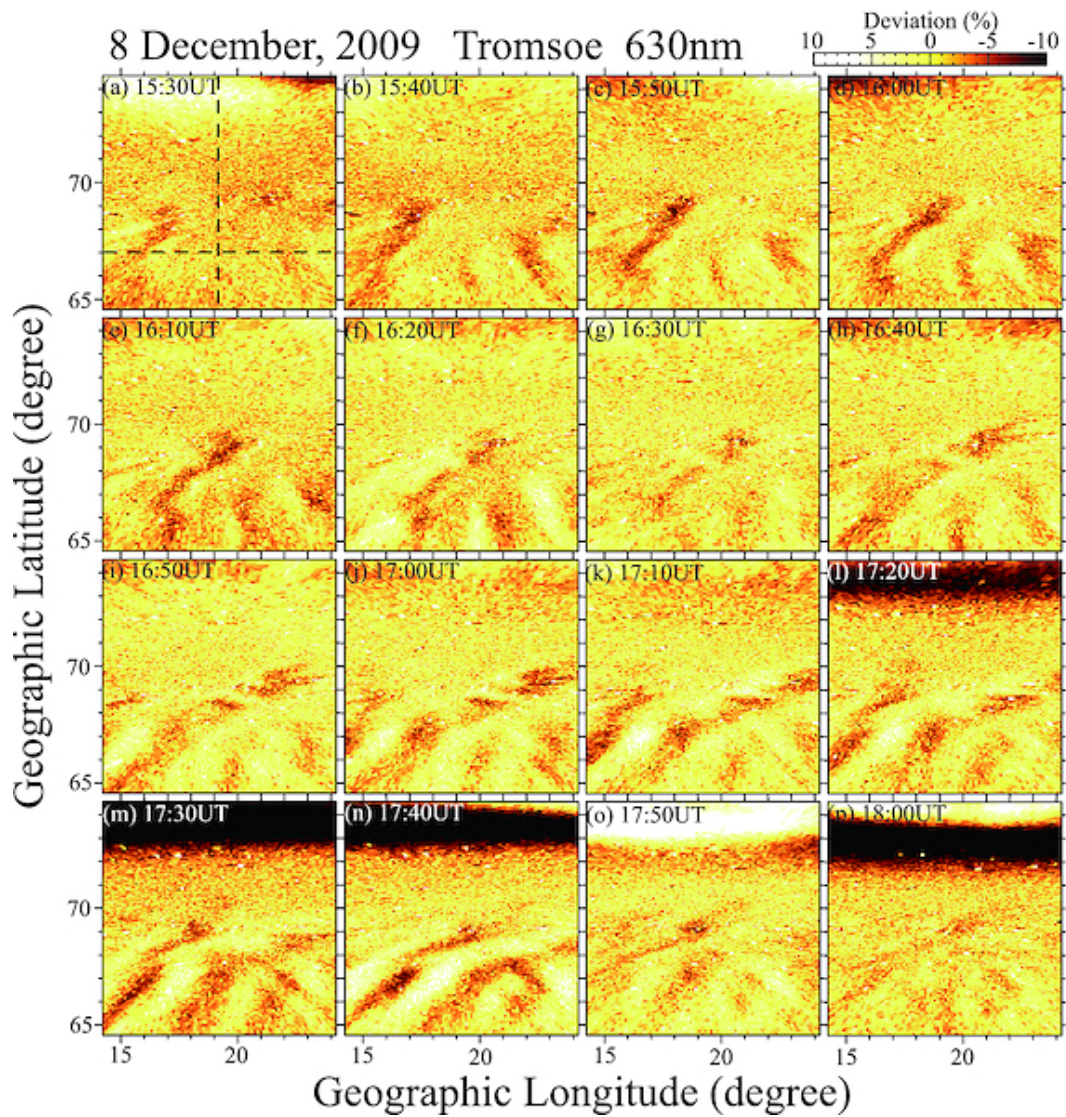


Figure 1.6 - TIDs in the polar Ionosphere: Airglow disturbances as observed from all-sky imager over Norway. Their presence is an indication of atmospheric and ionospheric disturbances since airglow is result of chemical reactions involving atmosphere and ionosphere.



SOURCE: Shiokawa et al. (2012)

2 AVAILABLE AND REQUIRED TOOLS

2.1 Measurements and Data processing

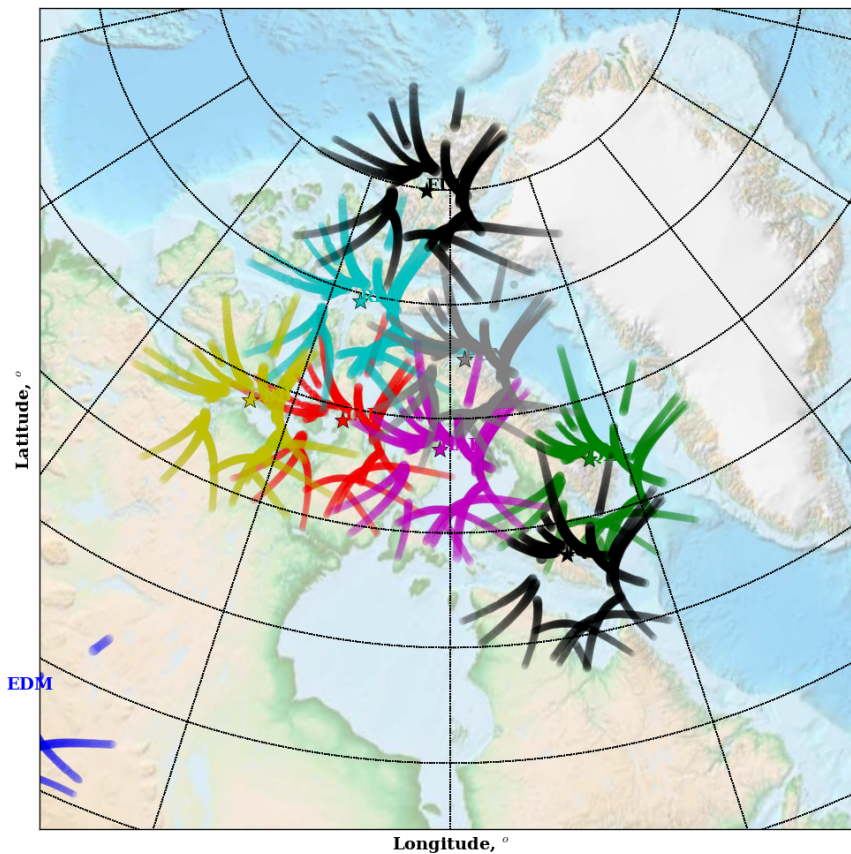
In recent years, the Canadian High Arctic Ionospheric Network (CHAIN) of GNSS receivers, that covers the latitude range of $80^\circ - 53^\circ$, has been used to scan the polar Ionosphere over Canada (JAYACHANDRAN et al., 2009a; JAYACHANDRAN et al., 2009b; WATSON et al., 2016). For example, Watson et al. (2016) have recently documented the imaging of polar cap/oval ionosphere, based on 6 year data statistics. They reported the TEC disturbances (more than 1 TECU) in the form of mesoscale ionization structures and focused on the daily/seasonal/annual occurrence rates and their spectral characteristics. They constructed the high resolution TEC maps, enabling them to link these disturbances accurately with the source of magnetospheric origin finally associating them to the morphology of the polar oval and precipitation dynamics. Noting the capacity of CHAIN to capture the mesoscale structures from the study by Watson et al. (2016), we focus on CHAIN data to attain our objectives.

We first select geomagnetically quiet day of 8 December 2009 for which the MSTIDs from all-sky imager over Norway is reported by Shiokawa et al. (2012). Capturing MSTIDs from CHAIN on this day with similar characteristics as those reported by Shiokawa et al. (2012) will validate the data analysis adopted in the present thesis. In the next step, exploration is widened by analysing CHAIN database during 2009-2016. The aim is to investigate the seasonal and solar cycle variations on the MSTIDs. For seasonal variation, the data on day 15 of each month in the year 2016 are examined. For solar cycle variation, data on day 15 of the month of intense MSTIDs are examined during 2009-2016. In the following, CHAIN network and TEC data processing are described:

2.1.1 CHAIN network

CHAIN network consisted of at least 9 receivers covering $80^\circ\text{N}-53^\circ\text{N}$ in latitude and $240^\circ\text{W}-310^\circ\text{W}$ in longitude over Canadian ionosphere. The spatial distribution of receivers and 6 hours (in between 12-18 UT) Ionospheric Piercing Point (projected at 300 km altitude) trajectories of satellites with elevation angle larger than 25° are shown in Figure 1. The time resolution of TEC data is 30 seconds.

Figure 2.1 - CHAIN receivers (denoted by stars) on 2009 and corresponding IPP trajectories projected at 300 km altitude.



2.1.2 TEC measurements

GNSS receivers of CHAIN network receives radio waves in L1 and L2 band from which the Slant-TEC is derived from the following definition:

$$\text{TEC}(t, i_r, i_{\text{prn}}) = \text{TEC}_\varphi + \langle \text{TEC}_p - \text{TEC}_\varphi \rangle_t \quad (2.1)$$

where:

$$\text{TEC}_\varphi = 9.52(\lambda_2\Phi_2 - \lambda_1\Phi_1); \text{TEC}_p = 9.52(P_1 - P_2) \quad (2.2)$$

Here subscripts 1 and 2 represent the measurements at frequencies L1=1575.42MHz and L2=1227.60 MHz, (P, Φ) are the pseudo range and phase measurements, $(\lambda_1=0.19, \lambda_2=0.244 \text{ meters})$ are the wavelengths of L1 and L2, (t, i_r, i_{prn}) are the time, receiver identification number and satellite PRN, $\langle \rangle_t$ is the time average.

In principle, TEC includes all kinds of variations associated with Ionospheric dynamics and satellites motions. However, the data resolution which is 30 seconds and data length from each satellite which is about 2 hours, limit the study to be more appropriate to micro/meso-scale variations. In other words, the data is ideal to study the mesoscale variations such as MSTIDs.

2.1.3 Keogram method

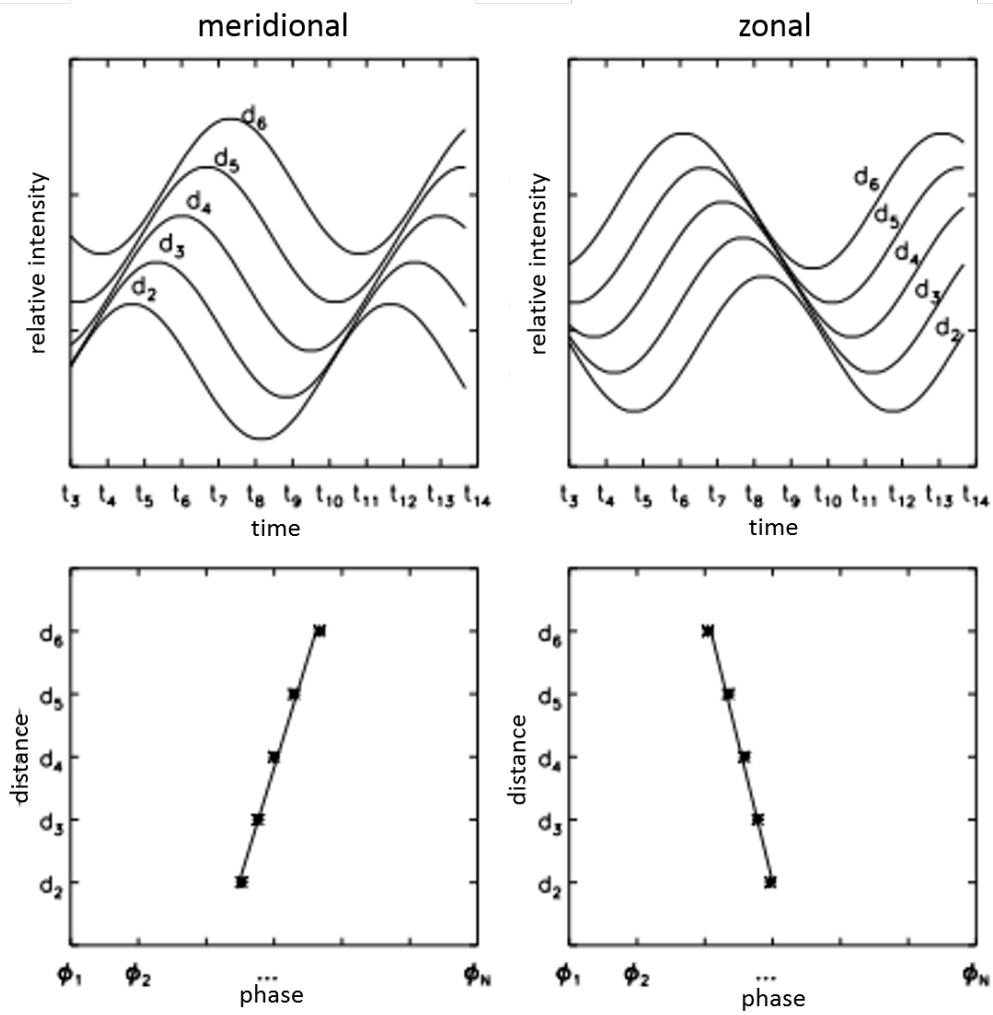
The TIDs propagation characteristics can be obtained through the keogram method. A keogram consists of a graphical representation of a data set in meridional (north-south) or zonal (east-west) slice as a function of time. With the keograms technique is possible to study separately the oscillations which occur from the zonal or meridional point of view. The keogram method has been used on a number of occasions to summarize wave activity in airglow image data (SWENSON et al., 2003; TAKAHASHI et al., 2009; TAYLOR et al., 2009; PAULINO, 2012) and TEC map (BARROS et al., 2018).

In Figure 2.2 can be seen five profiles of relative intensity extracted from meridional and zonal keograms. The periodicity of the oscillations is determined between the periodicities found in each of the lines. Periodicity will be considered valid when the same periodicity is detected at least considerable number of lines, for example in this case, three of five lines.

2.2 Numerical Experiments of MSTIDs

One of the widely accepted generation mechanism of MSTIDs, involve atmospheric waves excited by various forcings present in the polar oval and their subsequent coupling with the Ionosphere, as discussed in the introduction. Based on this mechanism, we perform Numerical Experiments, to simulate and interpret the observed characteristics of MSTIDs. Numerical experiments (NEs) are carried out by resolv-

Figure 2.2 - Adjustments for the horizontal (top) and the phase (bottom) keograms theoretical profiles.



SOURCE: Paulino (2012)

ing following governing equations of AGWs (KHERANI et al., 2016):

$$\frac{\partial^2 \vec{W}}{\partial t^2} = \frac{1}{\rho} \nabla(\gamma p \nabla \cdot \vec{W}) - \frac{\nabla p}{\rho^2} \nabla \cdot (\rho \vec{W}) + \frac{1}{\rho} \nabla(\vec{W} \cdot \nabla) p + \frac{\partial \Pi_{\text{visc}}}{\partial t} + \frac{\partial \Theta}{\partial t} \quad (2.3)$$

$$\frac{\partial \rho}{\partial t} + \nabla \cdot (\rho \vec{W}) = 0 \quad (2.4)$$

$$\frac{\partial p}{\partial t} + (\vec{W} \cdot \nabla)p + \gamma p \nabla \cdot \vec{W} = 0 \quad (2.5)$$

where \vec{W} is the amplitude of AGWs, $p = R\rho T$ is the pressure, (ρ, T) are the atmospheric mass density and temperature, Π_{visc} is viscous stress and (Θ) is the perturbed acceleration arising from the external forcing such as precipitation dynamics, tropospheric convection, polar vortex and so on.

The amplitude of AGWs, (\vec{W}) , couples with the ionosphere through equations (1.1-1.3) i.e.,

$$\nabla \cdot (J_w + J_d) = 0 \Rightarrow \nabla \cdot (\vec{\sigma} \cdot E) = \nabla \cdot J_w \quad (2.6)$$

$$U_\alpha = \mu_p(E + W \times B_o) + \mu_h(E + W \times B_o) \times \hat{b} + \mu_o(E \cdot \hat{b} + W \cdot B_o) \quad (2.7)$$

$$\frac{\partial n}{\partial t} + \nabla \cdot (nU_\alpha) = P + L \quad (2.8)$$

where,

$$J_w = \sigma_p(W \times B_o) + \sigma_h(W \times B_o) \times \hat{b} + \sigma_o W \cdot B_o$$

$$J_d = \sigma_p E + \sigma_h E \times \hat{b} + \sigma_o E \cdot \hat{b}$$

The NEs are carried out in the spherical coordinate (r, θ, φ) system in which three coordinates respectively represent altitude, latitude and longitude.

The forcing acceleration Θ in (2.2) is associated with the pressure perturbation (δp) or thermal perturbation (δT) in the following way:

$$\Theta = -\frac{1}{\rho} \nabla \delta p = -\frac{1}{\rho} \nabla (R\rho \delta T) \quad (2.9)$$

2.2.1 Joule heating associated with the auroral precipitation dynamics

The Joule heating due to the enhanced current (δj) from the precipitation (δn) in the E region has the following relation:

$$\frac{\delta j}{j_{oc}} = \frac{\delta n}{n_o} \quad (2.10)$$

where j_{oc} is the Cowling current. Therefore, the dissipated energy or heating rate (δQ) is given as follows:

$$\delta Q = \frac{1}{n_o} (\delta j \cdot E) \equiv \frac{1}{n_o} \frac{\delta n}{n_o} j_{oc} E \equiv \frac{1}{n_o} \frac{\delta n}{n_o} \sigma_p E^2 \equiv \frac{\delta n}{n_o} q \mu_p E^2 \quad (2.11)$$

or

$$\delta Q = \alpha \frac{\delta n}{n_o} J/s \quad (2.12)$$

Corresponding temperature change δT is given as follows:

$$\delta T = \frac{\delta Q}{k_B} = \frac{\alpha}{k_B} \frac{\delta n}{n_o} K/s \quad (2.13)$$

where:

$$\alpha = \frac{q}{B_o} \frac{\kappa}{1 + \kappa^2} E^2 e^{-(r-200)^2/\sigma^2} \sim \frac{10^{-19}}{0.2510^{-5}} \frac{\Omega}{\nu} E^2 e^{-(r-200)^2/\sigma^2} \quad (2.14)$$

Here (r) is the altitude. In the E region of polar oval, $E \sim 10$ mV/m, $\kappa = \Omega/\nu \sim 0.1$ and therefore,

$$\alpha \sim \frac{10^{-19} \times 10^{-5}}{0.2510^{-5}} \sim 0.5 \times 10^{-18} J/s \Rightarrow \frac{\alpha}{k_B} = 0.5 \times 10^5 \sim 5 \times 10^4 K/s \quad (2.15)$$

and therefore, the thermal perturbation in the E region is given as follows:

$$\frac{\delta T}{T_o} = \frac{5 \times 10^4}{T_o} \frac{\delta n}{n_o} \approx 10^3 \frac{\delta n}{n_o} e^{-(r-105)^2/\sigma^2} /s \text{ for } T_o = 500^\circ K \quad (2.16)$$

or

$$\frac{\delta T}{T_o} = 10^3 \frac{\delta f}{f_o} e^{-(r-105)^2/\sigma^2} \quad (2.17)$$

where ($f = nv$) is the proton/electron flux associated with the precipitation dynamics. Based on solar wind density ($\sim 10 \text{ cm}^{-3}$) of which 10% participates in the magnetotail, $\delta n \sim 1 \text{ cm}^{-3}$, $\delta f \sim 10^5 / \text{cm}^2 / s$ (PROLSS, 2004). Considering $f_o = n_o v_{alf}$,

the thermal perturbation can be estimated as follows:

$$f_o = n_o v_{\text{alf}} \gtrsim 10^4 \times 10^5 / \text{cm}^2 / \text{s} \Rightarrow \frac{\delta f}{f_o} \lesssim 10^{-4} \Rightarrow \frac{\delta T}{T_o} \lesssim 10^{-1} e^{-(r-105)^2 / \sigma^2} \text{ during daytime} \quad (2.18)$$

$$f_o = n_o v_{\text{alf}} \lesssim 10^3 \times 10^5 / \text{cm}^2 / \text{s} \Rightarrow \frac{\delta f}{f_o} \gtrsim 10^{-3} \Rightarrow \frac{\delta T}{T_o} \gtrsim 1 e^{-(r-105)^2 / \sigma^2} \text{ during nighttime} \quad (2.19)$$

Therefore, the peak heating rate is larger during nighttime owing to the lesser background density or current. This makes the precipitation dynamics more favourable source for AGWs during nighttime.

It is evident that the thermal perturbation above has Gaussian variation in altitude (r). In general, it also has Gaussian variation in the horizontal plane (θ, φ) with $\sigma = 10^\circ$ (PROLSS, 2004). In other words, the ratio $\delta T / T_o$ above is modified as follows:

$$\frac{\delta T}{T_o} = \beta e^{-(r-105)^2 / \sigma^2} e^{-(\theta-\theta_o)^2 / 10^2} e^{-(\varphi-\varphi_o)^2 / 10^2} = \beta S(r, \theta, \varphi) \quad (2.20)$$

Since the MSTIDs have spectral peak at period ~ 0.5 -1 hours, the above expression is modified by temporal variation as follows:

$$\frac{\delta T}{T_o} = \beta S(r, \theta, \varphi) e^{-(t-45)^2 / 45^2} \quad (2.21)$$

where $0.1 \leq \beta \leq 1$, in other words, the thermal disturbance during precipitations can reach 10%-100% of the ambient temperature.

3 MSTIDS ON DAY 08 OF DECEMBER 2009

Medium scale Traveling Ionospheric Disturbances (MSTIDs) are wavelike perturbations in the F region ionospheric density and electric field that propagate with horizontal wavelengths of 100-300 km and periods of 15 min – 1 hours (FRANCIS, 1974). They have been detected at various latitudes of which the high-latitude MSTIDs is of present interest. They are observed during both geomagnetically quiet and disturbed periods.

Noting the capacity of CHAIN to capture the mesoscale structures from the study by Watson et al. (2016), we set our objective to study the propagation characteristics of MSTIDs in the polar ionosphere. We select the geomagnetically quiet day of 8 December 2009 for which the nightside MSTIDs from all-sky imager over Norwegian ionosphere is reported by Shiokawa et al. (2012). They found the presence of nighttime MSTIDs in the $75^\circ - 65^\circ$ latitude range that appeared around 15:30UT in response to auroral brightening and further intensified around 17:30 UT. These MSTIDs were found to propagate equator-eastward with the average velocity of ~ 60 -100 m/s and their wavefronts were aligned in Southwest-Northeast (SW-NE) direction.

3.1 CHAIN network and data analysis

In Figure 3.1a, we present the TEC variation registered at Cambridge Bay GPS receiver (latitude = 68.97°). The average TEC variation (red curve) is obtained by averaging the TEC (grey curves) variation deduced from all satellites at each instant of time. In Figure 3.1b, the wavelet spectrum of average TEC is shown.

The temporal-spatial distributions of the IPP trajectories of two PRNs=10,16 are used to construct the keograms of Δ TEC in Figures 3.2-3.3. The Δ TEC is obtained by applying the band pass-filter along the temporal variation of TEC. Both latitude and longitude keograms can be constructed by organizing the IPP trajectories along latitude and longitude, respectively. In Figure 3.2, the latitude keograms of Δ TEC for four frequency bands in 0.2 – 1.11mHz, as indicated at the top of each panel, are shown. In figure 3.3a, the latitude keogram corresponding to the 0.48 – 0.37mHz is replotted. In Figure 3.3b, the longitude keogram corresponds to the same band-pass filter is plotted. In Figure 3.3(c-d), the latitude and longitude keograms constructed using all PRNs are shown. In Figure 3.4, the snapshots of Δ TEC map at 4 chosen

times are shown. These maps are constructed by 4 points interpolation, employing the nearest point method.

3.2 Results and Discussion

From the wavelet spectrum in Figure 3.1, we note the surge of large spectral power (encompassed by a rectangle) of TEC in the 0.4 mHz-0.8 mHz frequency range (or 40-20 minutes) during 13-18 UT, having largest amplification near 15:00 UT (noon-time) and again re-surge around 17:30 UT (post-noon time). These temporal and spectral characteristics and time of appearance of spectral power are very similar to those reported by [Shiokawa et al. \(2012\)](#) for the night-side MSTIDs on the same day. This is the first indication that the amplified waveforms of Δ TEC encompassed as rectangle in Figure 3.1, are associated with the MSTIDs though their propagation nature is yet to be confirmed.

The latitude keograms in Figure 3.2 reveal presence of strong Δ TEC in 0.48 – 0.37 mHz, in comparison to other frequency bands. This confirms the spectral characteristics noted in Figure 3.1 and suggests that Δ TEC has similar spectral characteristics over entire polar ionosphere since keograms in Figure 3.3 covers the latitude range of $60^\circ - 80^\circ$.

The keograms in Figure 3.3 (a-b) facilitate us to infer the propagation characteristics of Δ TEC, by identifying the aligned phases. Few such propagations are identified in Figure 3.3(a-b), denoted by black lines. The slope of these lines in latitude and longitude keograms are $\sim 250-500$ m/s and $\sim 1-2$ km/s, respectively, suggesting the disturbances to propagate equatorward-eastward with these velocities. We note that this propagation pattern is noted around 15 UT i.e., at the time of large amplification of Δ TEC in Figure 3.3, when surge of nightside MSTIDs is reported by [Shiokawa et al. \(2012\)](#)). Therefore, the disturbance pattern in Figure 3.3(a-b) can be attributed to the dayside MSTIDs. The eastward velocity $\sim 1-2$ km/s is extremely large to be explained during quiet-time. However, in the presence of longitudinally wide wavefront, such large velocity is possible if the wavefront is slightly tilted with respect to the east-west axis, having aligned in SW-NE direction, as also reported by [Shiokawa et al. \(2012\)](#). In that case, the wide wavefront passes rapidly through narrow latitude band that resides four longitudinally separated receivers.

Moreover, during substorm, the TEC signature associated with the particle precip-

itation are reported to have expansion velocity of $\sim 1\text{-}2$ km/s (WATSON et al., 2011). Both equatorward and eastward velocities in the present study falls in this range. This suggests the energetic nature of quiet-time MSTIDs in Figure 4 similar to those observed during substorm. This also permits us to explore the possibility of their association with the particle precipitation in the polar ionosphere. In this context, it is to be mentioned that the Shiokawa et al. (2012) have reported the strengthening of auroral activities during the surge of nightside MSTIDs on this day. Watson et al. (2016) have also associated the high occurrence rate of noon-time mesoscale TEC disturbances to the precipitation mechanism under winter time low conductivity condition. Therefore, the noon-time MSTIDs presented in Figure 3.3 are possibly associated with the dynamics triggered by precipitation in the auroral region.

Watson et al. (2016) also reported the post-noon mesoscale disturbances and associated them to the precipitation mechanism from the magnetospheric boundary regions and the plasma sheet. The post-noon surge (around 17:30UT) of ΔTEC in Figure 3.1 may have such association with the precipitation. In Figure 3.3(a-b), we do not notice the post-noon surge of ΔTEC owing to the trajectory geometries of chosen PRN=10,16. To examine such surge in keograms, we construct the accumulative latitude and longitude keograms in Figure 3.3(c-d) by considering all PRNs during 12-18 UT. We note the surge of another set of phase fronts during post-noon hours, as also noted by Shiokawa et al. (2012) for the nightside MSTIDs. This post-noon MSTIDs may also have association with the precipitation dynamics of the magnetospheric boundary layers and plasma sheet, as suggested by Watson et al. (2016).

As noted above, the dayside MSTIDs in the present study appear during 13-18 UT in the latitude range of $75^\circ - 60^\circ$ when the presence of their nightside counterpart is reported by Shiokawa et al. (2012). The simultaneous occurrence of dayside and nightside MSTIDs suggests the involvement of common driving source (such as the precipitation mechanism) for their generation, located somewhere in the polar cap region, as suggested by Shiokawa et al. (2012). This finding also raise the possibility of involvement of large-scale generation mechanism as also proposed by Frissell et al. (2016). The propagation direction of the dayside MSTIDs in Figure 3.3 is similar to their nightside counterparts i.e. they propagate toward equator-eastward. On the other hand, their propagation speed is much larger than their nightside counterpart. This difference may arise from various reasons notably among them are the day-night differences in the ambient ionospheric/atmospheric conditions and their subsequent effects on the underlying generation mechanisms.

In Figure 3.4, we present the snapshots of ΔTEC distribution constructed from spatial distribution of IPP. We note the presence of wave-fronts which are aligned parallel to the green line, in Southwest-Northeast direction, as also observed by [Shiokawa et al. \(2012\)](#). The wavelengths and propagation of these wavefronts can not be quantified from these snapshots as it requires more dense GNSS network.

Noting the presence of MSTIDs from TEC measurements, we further probe their presence by analysing the vertical magnetic field (b_z) variations measured from the ground-based magnetometers of CANadian Magnetic Observatory System (CAN-MOS). In Figure 3.5(a), the magnetic disturbances (Δb_z) obtained by de-trending b_z are shown. In Figure 3.5(b), Δb_z at Cambridge Bay and ΔTEC at three surrounding stations are shown. We note the surge of Δb_z of ~ 3 nT during the surge of ΔTEC in the surrounding of Cambridge Bay. This strong correlation suggests the high degree of association between Δb_z and ΔTEC disturbances associated with the MSTIDs. [Shiokawa et al. \(2012\)](#) have also found such correlation and shown the occurrence of nightside MSTIDs in direct response to the ionospheric electric field associated with the magnetic perturbation and auroral brightening at the poleward edge of the auroral region. Therefore, the dayside MSTIDs observed in the present study occur in direct response to the ionospheric dynamics in the auroral region. Another possibility is the Acoustic-Gravity waves (AGWs) which are known to be responsible for the high-latitude MSTIDs ([RICHMOND, 1978](#)). These AGWs may arise from the atmospheric dynamics such as the polar vortex and/or the ionospheric dynamics such as the enhanced current disturbance during precipitations ([FRISSELL et al., 2016](#); [SHIOKAWA et al., 2012](#); [WATSON et al., 2016](#)). In the present study, the ionospheric dynamics seems to be the likely candidate while the atmospheric dynamics remains unexplored.

3.3 Summary

The present study focuses on the detection of MSTIDs over Canadian auroral ionosphere, deduced from the Total Electron Content (TEC) data obtained using CHAIN network of GNSS receivers. We found their spectral peak in 0.48-0.37 mHz i.e. in 35-45 minutes periodic range in the entire polar region. Their presence are identified as the amplified waveforms in the filtered TEC data, appearing during 13-18 UT in $75^\circ - 60^\circ$ latitude range that propagate equator-eastward. The important result of the present study is that these characteristics are similar to their nightside counterpart observed on the same day over Norwegian ionosphere by [Shiokawa et al. \(2012\)](#).

The simultaneous presence of the dayside and nightside MSTIDs suggests the common driving source involved in their generation and also of their global nature which are other important outcomes of the present study. The equatorward velocity of dayside MSTIDs is noted to be in the range of $\sim 250\text{-}500$ m/s which is within the known range of MSTIDs. This estimate is different from the velocity of ~ 60 m/s reported for their nightside counterpart by [Shiokawa et al. \(2012\)](#) which may be attributed to the day-night differences in the ambient conditions and subsequent effects on the underlying generation mechanisms. Moreover, their eastward velocity comes out to be $\sim 1\text{-}2$ km/s and such extremely large velocity is interpreted as the apparent velocity caused by the passage of longitudinally wide wavefront with slight tilt from east-west having aligned in SW-NE direction, as also reported by [Shiokawa et al. \(2012\)](#). These MSTIDs appear during the surge of small magnetic perturbations of ~ 3 nT in the auroral region, as registered from the ground-based magnetometer, a feature again reported for the nightside counterpart. Based on previous works by [Shiokawa et al. \(2012\)](#) and [Watson et al \(2016\)](#), we argue these MSTIDs to be associated with the precipitation dynamics in the polar region.

Figure 3.1 - TEC measurements from the station Cambridge Bay located at $68.97^{\circ}N$: (Upper panel) The gray curves and the superimposed red curve represents TEC from each PRN and the average TEC over all PRN respectively (Lower panel): The wavelet spectra of TEC is shown. The rectangle frame covers the time zone of interest.

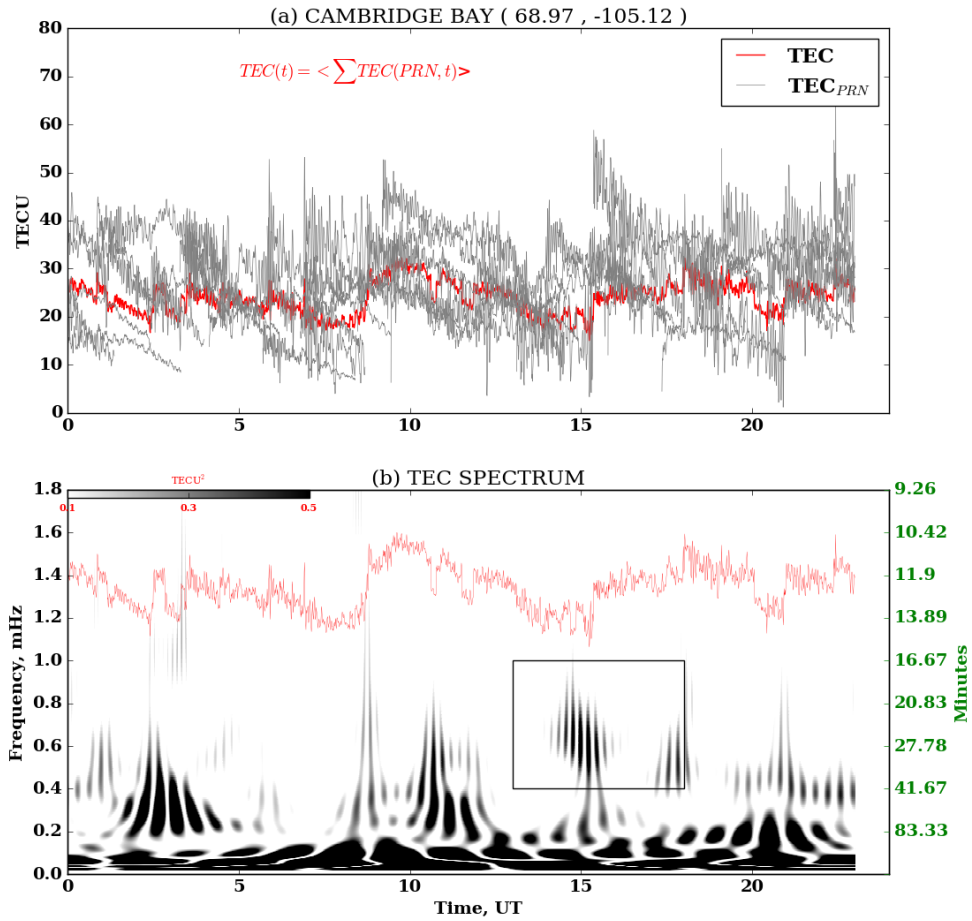


Figure 3.2 - The latitude keograms for 4 frequency bands, 15-25, 35-45, 55-65 and 75-85 minutes, respectively.

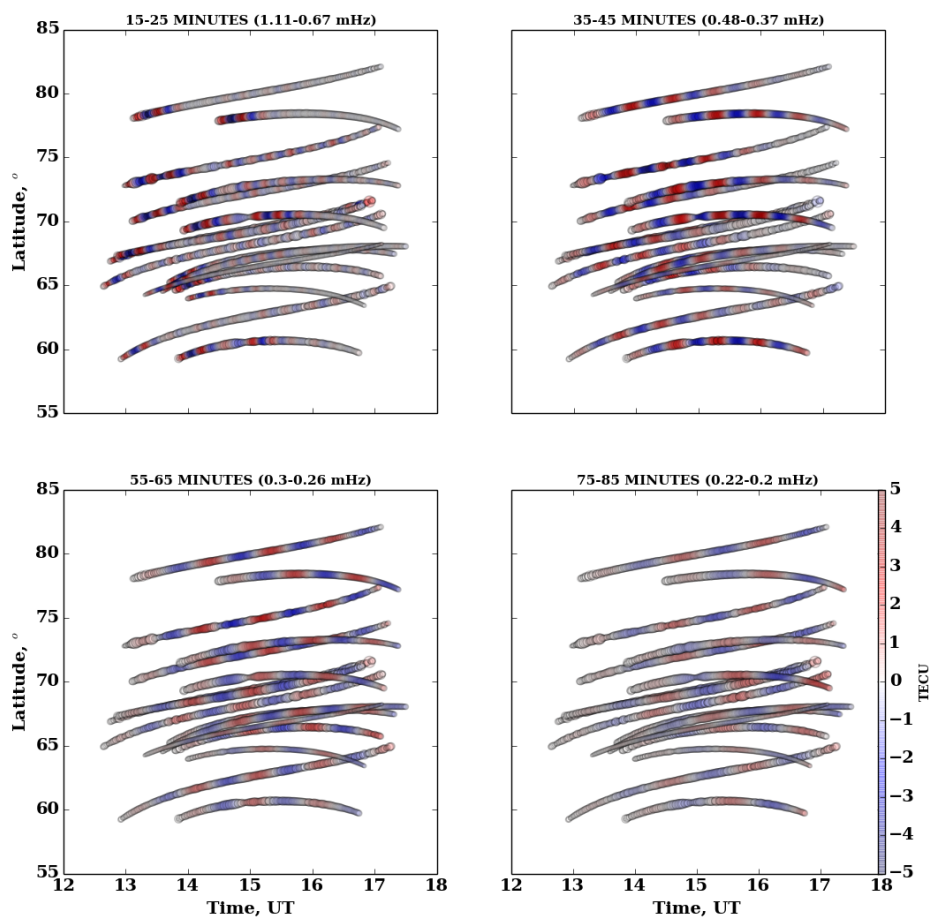


Figure 3.3 - (a-b) Latitude and longitude keograms constructed by considering the IPP trajectories of PRNs=10,16. (c-d) Latitude and longitude keograms constructed by considering the IPP trajectories of all PRNs. In the latitude and longitude keograms, two green lines with different slopes (as denoted by numbers in green colors) are drawn. Also drawn are the black lines along which phases are aligned i.e. they are few identified wavefronts.

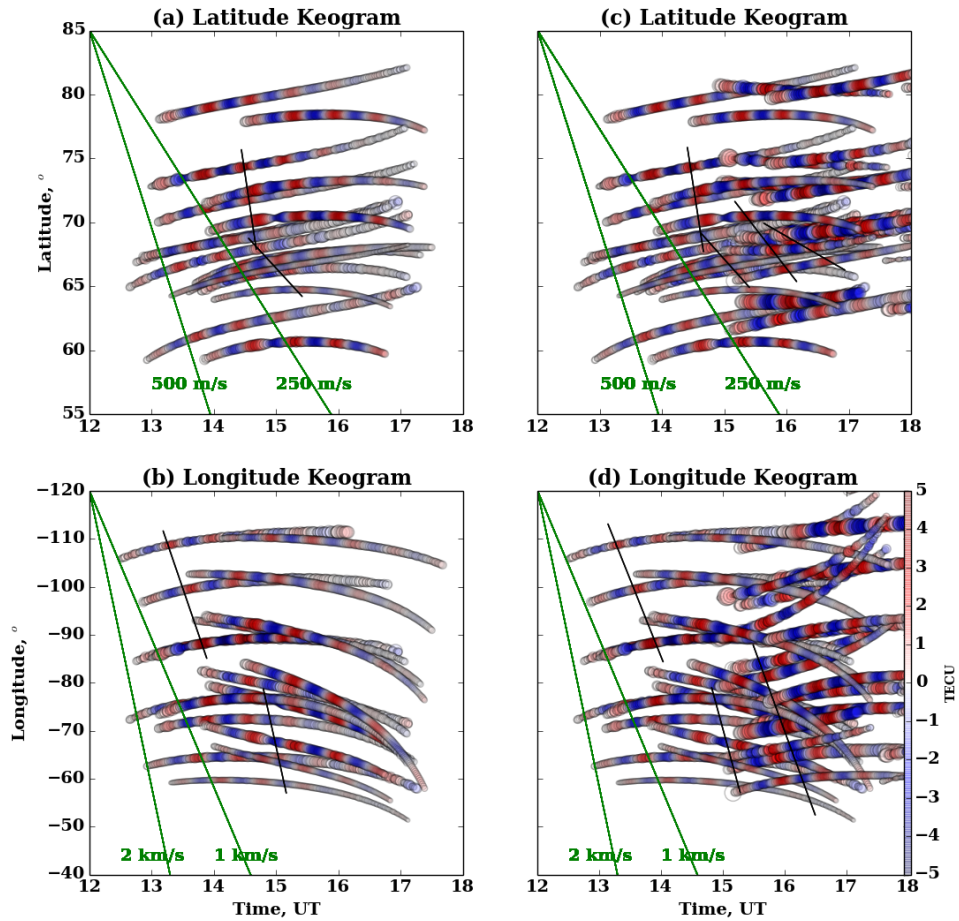


Figure 3.4 - Snapshots of ΔTEC at four chosen times, as mentioned at the top of each panel. These maps are constructed by 4 point interpolation of original IPP points. In each panel, a green line is drawn along which wavefronts are aligned and successively distancing away equator-eastward.

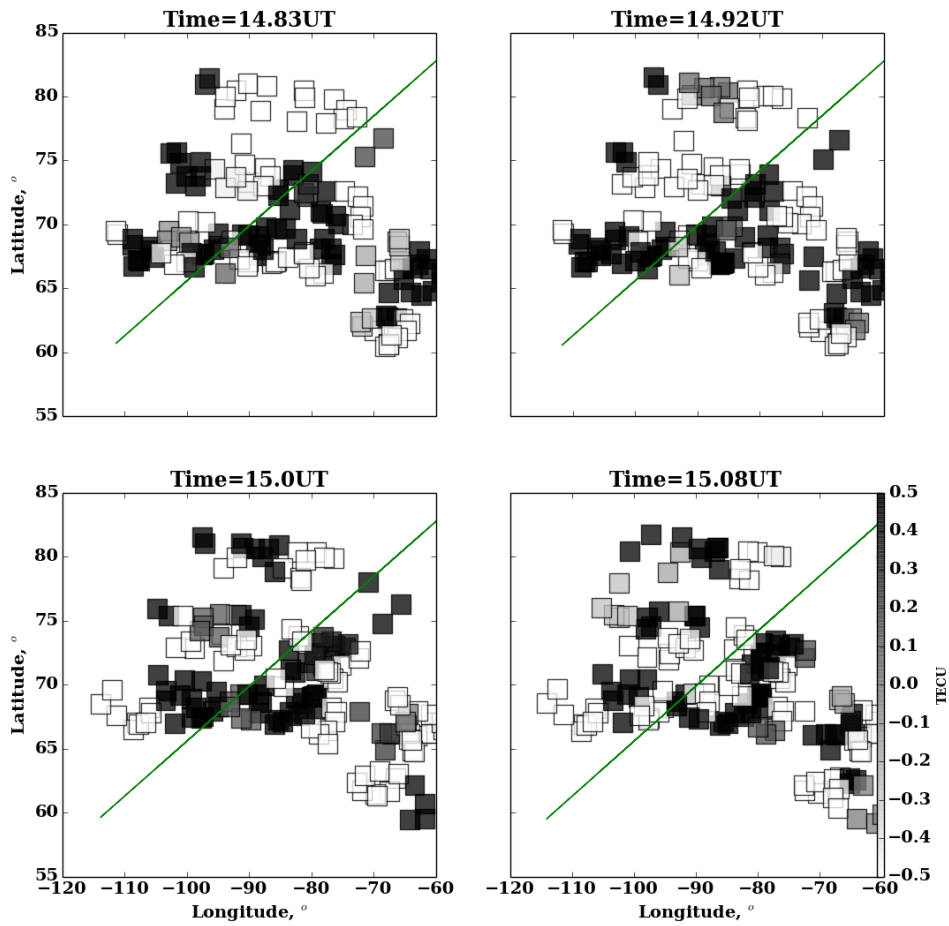
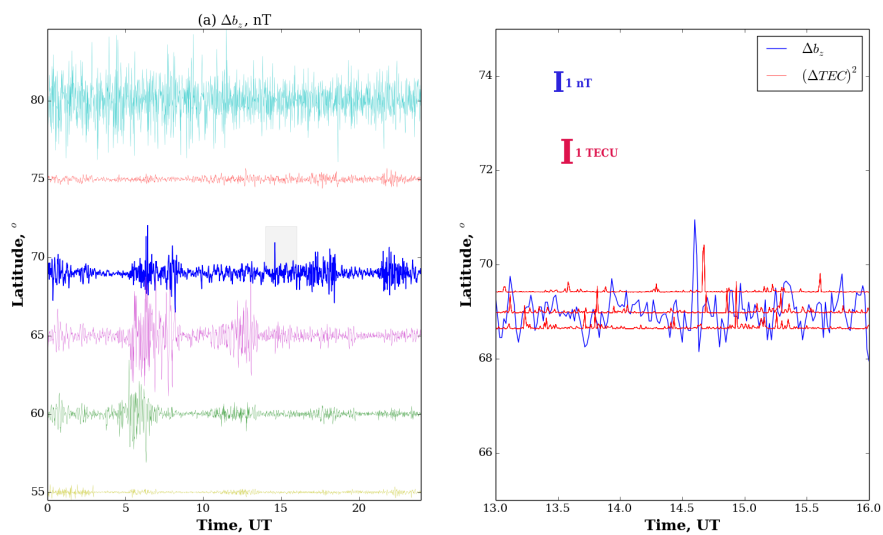


Figure 3.5 - (a) Magnetic field disturbances Δb_z obtained by de-trending the vertical magnetic field component measured from CANMOS magnetometer network are shown. (b) Δb_z (blue curve) at Cambridge Bay and ΔTEC^2 (red curves) at three stations surrounding Cambridge Bay are shown.



4 SEASONAL AND SOLAR-FLUX VARIABILITIES OF MSTIDS

Past studies have revealed the diurnal, seasonal and solar-flux variabilities of the characteristics of MSTIDs at high latitudes (HERNÁNDEZ-PAJARES et al., 2012; WATSON et al., 2016). Interestingly, these variabilities are similar to the MSTIDs at mid and low latitudes. These studies have found that the majority of the most intense MSTIDs activity occurs at daytime during fall/winter and nighttime during spring/summer, at high latitudes. Moreover, their occurrence is modulated in intensity by the solar cycle such that maximum (minimum) occurrence correspond to high (low) solar flux (HERNÁNDEZ-PAJARES et al., 2012).

In this chapter, seasonal and solar cycle effects on the occurrence and propagation characteristics of MSTIDs are presented, using CHAIN network. The four seasons, namely winter (December-March), Summer (June-September) and fall/springs over Candian polar Ionosphere present different states of Ionosphere and therefore are expected to affect MSTIDs dynamics.

4.1 Results and Discussion

In Figure 4.1, the distribution of GNSS receivers of CHAIN network are shown for 2015 onwards when it is consisted of more than 20 receivers. This allows higher space-resolute TEC data, in comparison to the earlier years. In order to study the seasonal effects on MSTIDs, winter day of 15 January, summer day of 15 July, equinox days of 15 April and 15 October are considered as representative days. They all belong to same year 2016 that represents the low solar flux year.

The data analysis presented in the previous chapter is employed to obtain the Δ TEC disturbances for the statistical study in this chapter. The results are presented in the form of latitude-keograms in Figures 4.2-4.4 for years 2016-2017 and in Figure 4.5 for year 2014. We note that the keograms of 2016-2017 have much denser Δ TEC distribution, in comparison to 2014 and also in comparison to the keograms in the previous chapter.

4.1.1 Seasonal variability

From Figures 4.2-4.3, it is noted that summer day has strongest MSTIDs compared to the winter day while equinox days have weakest MSTIDs. In fact, on equinox days, no clear wavefront propagation is present, indicating the absence of MSTIDs. On summer and winter days, wavefront propagations are evident, suggesting the presence of MSTIDs. It is noted that the propagation is both equatorward/poleward with the propagation velocity in the range of 250 m/s-500 m/s for winter and summer MSTIDs. Moreover, they cover almost 30° in latitude during their propagation and majority of them have strongest amplitudes in polar cap latitudes. Both summer and winter MSTIDs last for almost 2 hours and four such surge occur in 24 hours i.e., MSTIDs have occurrence periodicity of ~ 6 hours.

4.1.2 Solar-flux variability

In Figures 4.4-4.5, winter and summer MSTIDs in another low solar flux year of 2017 and high solar flux year of 2014 are presented. The MSTIDs in 2017 confirm the characteristics noted in 2016. In 2014, owing to less number of receivers in CHAIN in comparison to 2017, Δ TEC distribution is less denser. However, propagation characteristics i.e., the presence of MSTIDs is still evident. Most of the characteristics in 2014 are in confirmations with those noted in 2016 except that the winter MSTIDs are stronger in 2014 in contrast to the stronger summer MSTIDs in 2016-2017. In fact, we note that the amplitudes of summer MSTIDs remain unaltered in high and low solar fluxes. However, amplitudes of winter MSTIDs undergoes significantly change from high to low solar flux years.

Most of the characteristics of MSTIDs mentioned above are reported for the first time in detail and some of these characteristics are different from those reported in the past studies.

Past studies of mesoscale structures such as MSTIDs (Watson et al, 2016), poleward moving polar patches and aurora (JAYACHANDRAN et al., 2009a), pulsating aurora (WEATHERWAX et al., 1997) revealed stronger amplitudes during winter, moderate during equinoxes and weaker during summer. The present study finds strongest MSTIDs in winter 2014 in confirmation with the past studies. However, it also reveals weaker (weakest) MSTIDs in winter (equinoxes) in low solar flux year of 2016-2017, in contrast to the past studies. Therefore, solar flux has diverse effects on the am-

plitudes of winter MSTIDs and has insignificant effects on summer MSTIDs. This is expected since the ionosphere is more responsive/reactive to change in solar inputs owing to relatively low level winter ionospheric dynamics, in comparison to summer dynamics.

In the past studies, the mesoscale structures are either reported to propagate poleward, in case of polar patches/aurora or their propagation characteristics remained unexplored, in case of MSTIDs/pulsating aurora. The present study reveals both poleward and equatorward propagating MSTIDs with velocity in the range of 250 m/s-500 m/s and latitude coverage of about 30° that suggest their robust nature. They are more intense in poleward suggesting the polar oval dynamics to participate in their generation and to provide favourable conditions for their propagation. The propagation characteristics in such details are reported for the first time from the present study.

Another detailed characteristics from the present study is the presence of various time scales associated with the MSTIDs. Three such scales are found: time period \sim 20-40 minutes, survival time scale \sim 1-2 hours and occurrence time scale \sim 6 hours. Presence of such periodicities suggests both tidal and AGWs modes to be involved in the processes, apart from the electrodynamical processes associated with the solar wind-Magnetosphere coupling.

Study by [Hernández-Pajares et al. \(2012\)](#) has revealed that the majority of the most intense MSTID activity occurs at daytime during winter and nighttime during summer, at high latitudes. In contrast to this, Figure 4.2 shows the weakest nighttime summer and day-time winter MSTIDs which is due to the fact that during summer and winter, night and day over Canada are respectively too short to produce well developed MSTIDs in the polar Ionosphere. This contrast is explained as follows: from Figure 4.2, it is evident that winter and summer MSTIDs have similar Universal Time variabilities. It raises a possibility that the observed MSTIDs are generated from the source that is available to both day and night. This is possible at high latitudes in the polar cap or oval regions owing to their extremely less diametral circular areas. Therefore, the observations presented in Figure 4.2-4.3 suggest the location of origin of the MSTIDs to be in the polar cap and oval. This is also coherent with the results from the observations of MSTIDs on 8 of December 2009, as presented in the previous chapter.

4.1.3 Seasonal and solar-flux variabilities of Spectral characteristics

In Figures 4.6-4.9, Spectrograms of TEC are presented for 12 months (12 panels in each figure) during 2013-2016. The data belongs to receiver at Cambridge Bay (CBB) which is located in the polar oval region.

As noted in the previous chapter that the MSTIDs cover the frequency range between 0.2-0.8 mHz, we focus on Δ TEC disturbances in this frequency range. We note that the MSTIDs are intensified around summer day (day 166 or 167) irrespective of year. Also, MSTIDs are stronger in high solar-flux year 2013 as compared to low solar-flux year 2016. It is noted that the spectral range of MSTIDs are much wider during summer and high solar flux year, in comparison to winter and low solar flux year. Most of strong MSTIDs are concentrated in the frequency range of 0.2-0.3 mHz suggesting their oscillation periods to be about 1 hours.

These characteristics strongly link MSTIDs activities to the solar driven dynamics in the polar ionosphere. The precipitation dynamics associated with dayside cusp and/or nightside boundary layers, are primary sources for the mesoscale structures in the polar ionosphere (WATSON et al., 2016). The equatorward propagation of MSTIDs are explained based on the Joule heating associated with the precipitation dynamics (RICHMOND, 1978). The poleward propagating MSTIDs, on the other hand, may have origin in the mid latitude and possibly driven by tropospheric convections (HERNÁNDEZ-PAJARES et al., 2012). The observations of both poleward and equatorward MSTIDs in the present study, therefore suggest the involvement of different sources.

The wide latitudinal coverage of order of 30° is another interesting aspect of the present study that promotes the possibility that the high-latitude MSTIDs can disturb the mid-latitude Ionosphere. It also demonstrates that the high-latitude MSTIDs find favourable conditions to propagate long distance in spite that they travel through different ionospheric states. Apart from the present study, only another study that reports the long distance propagating MSTIDs is by Ishida et al. (2008) that used the Super DARN radar to image the Ionosphere. Based on TEC measurements, the present study is possibly the first to report the long distance propagation.

4.2 Summary

This chapter presents following new aspects of MSTIDs:

1. Both equatorward and poleward propagating MSTIDs are simultaneously present in the high-latitude Ionosphere,
2. MSTIDs are strongest in summer (winter) in low (high) solar-flux conditions,
3. Strongest MSTIDs have periods of 1 hours,
4. Spectral range of MSTIDs are wider during summer and high solar-flux condition,
5. MSTIDs propagate long distance in latitude and disturb the mid-latitude Ionosphere,
6. The present study demonstrates the efficiency of relatively low dense GPS network such as CHAIN to monitor the MSTIDs.

Figure 4.1 - CHAIN from 2015 onwards. The black stars represent receivers of CHAIN network before 2015.

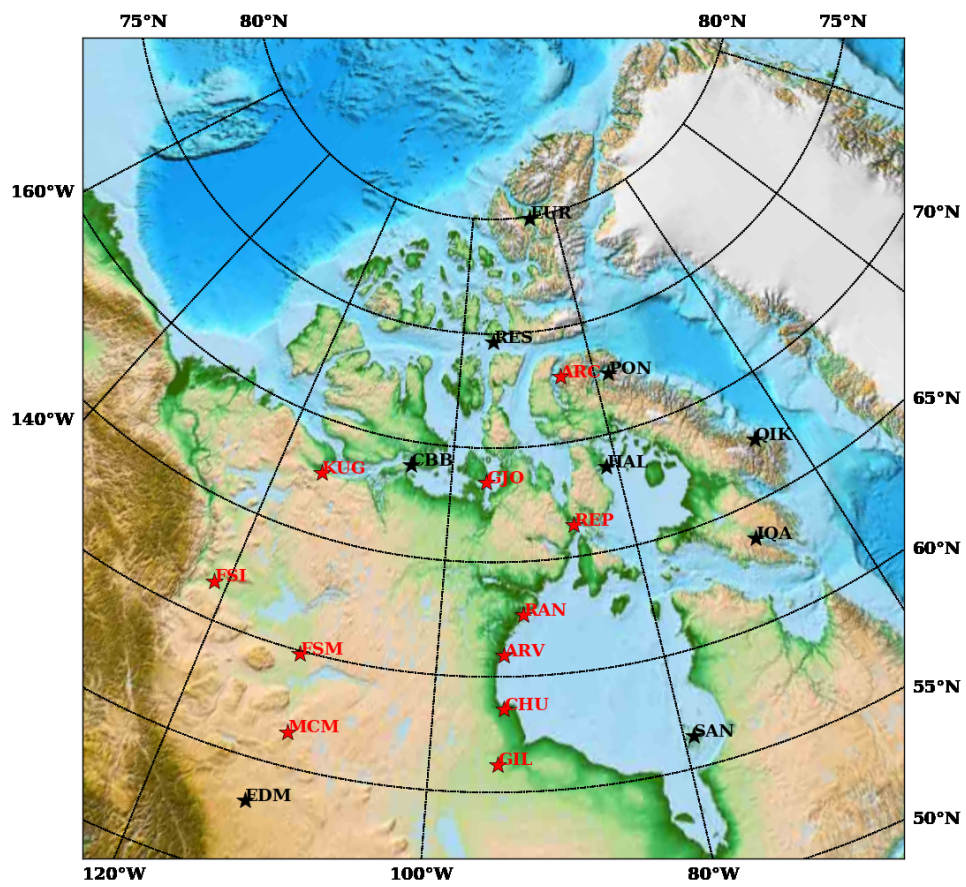


Figure 4.2 - Seasonal Variabilities on year 2016: Latitude keograms of Δ TEC on winter and summer 2016. The black squares indicate the sunrise time and the red circles indicate the sunset time

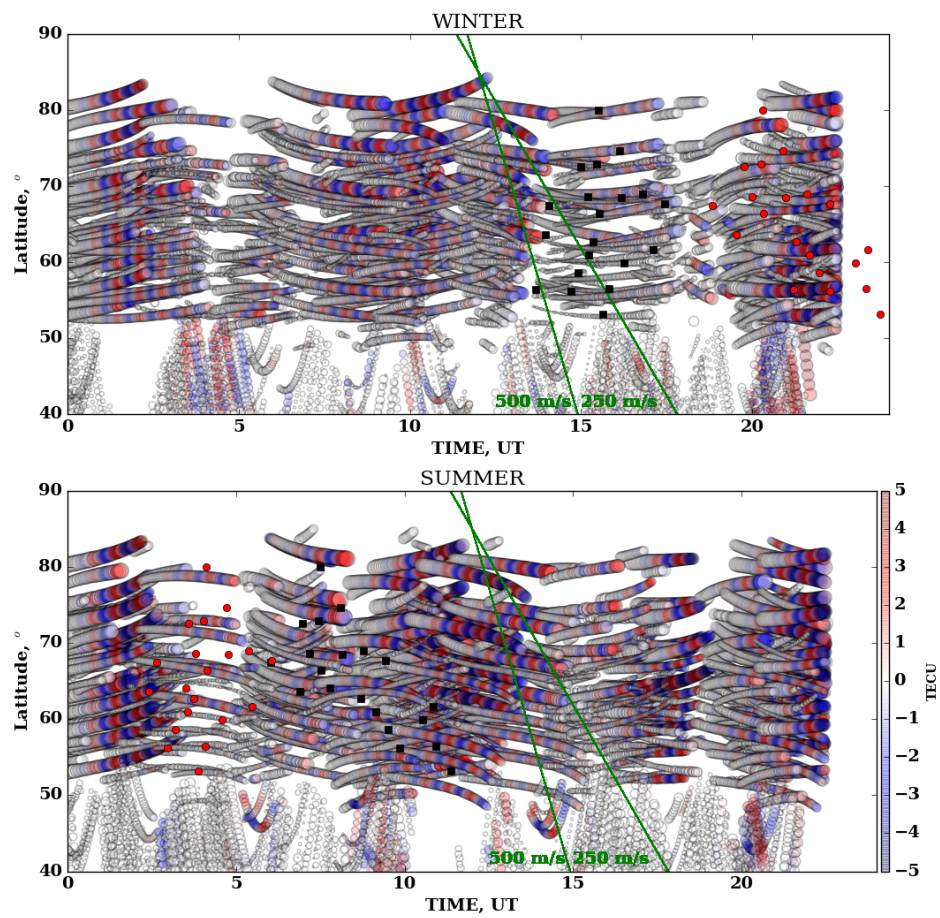


Figure 4.3 - Seasonal Variabilities on year 2016: Latitude keograms of Δ TEC on spring and winter equinoxes 2016. The black squares indicate the sunrise time and the red circles indicate the sunset time.

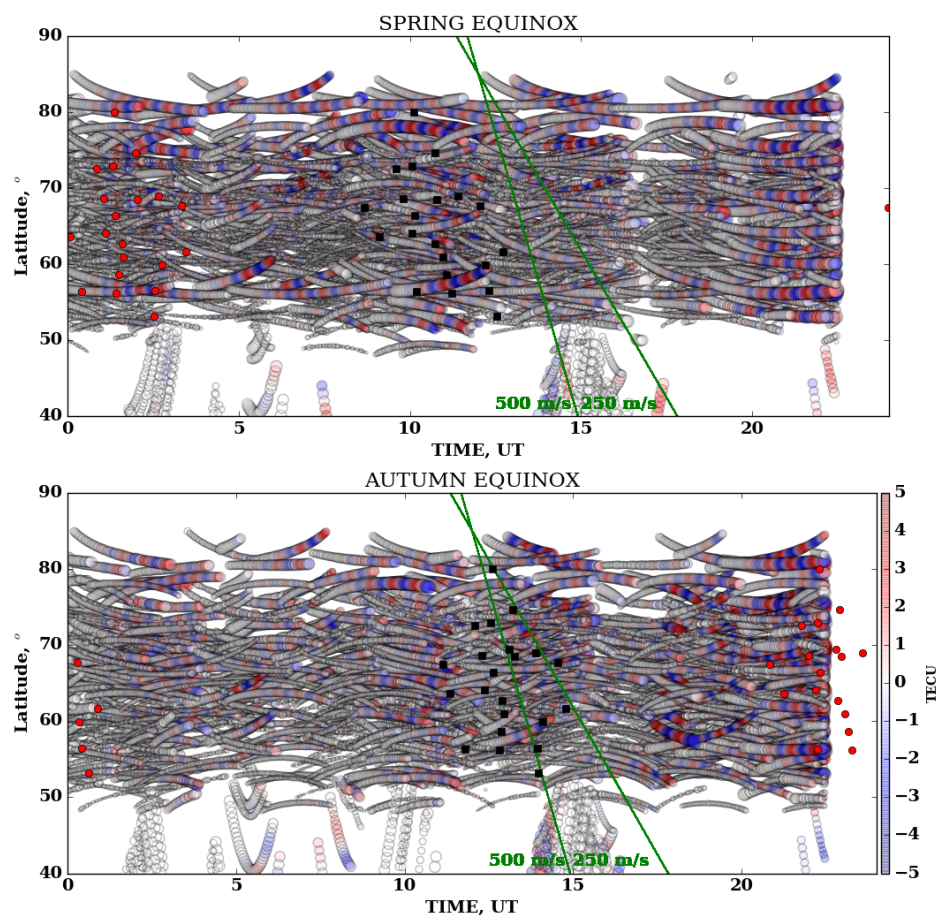


Figure 4.4 - Latitude keograms of Δ TEC on winter/summer on low-solar flux year 2017. The black squares indicate the sunrise time and the red circles indicate the sunset time.

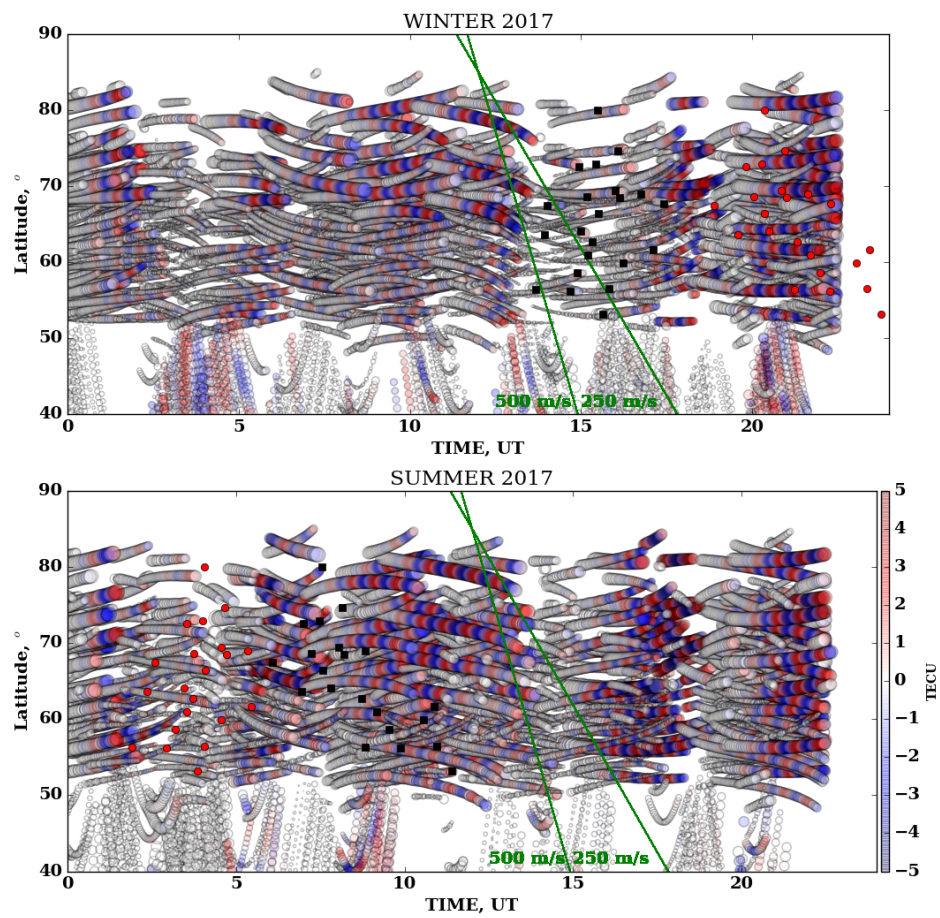


Figure 4.5 - Latitude keograms of Δ TEC on winter/summer on high solar flux year 2014. The black squares indicate the sunrise time and the red circles indicate the sunset time.

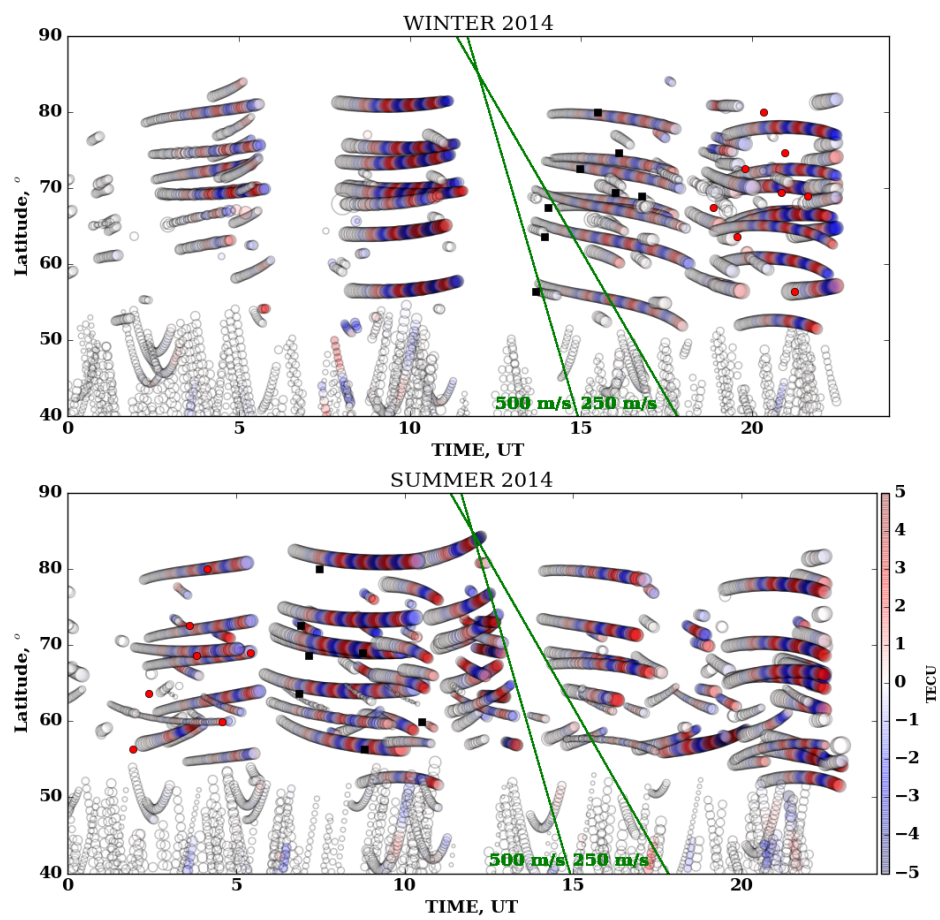


Figure 4.6 - Spectrogram of TEC data derived from receiver at CambridgeBay (CBB) on year 2013. The TEC data on representative days of 12 months are plotted in panels and the number of day is denoted at the top of each panel.

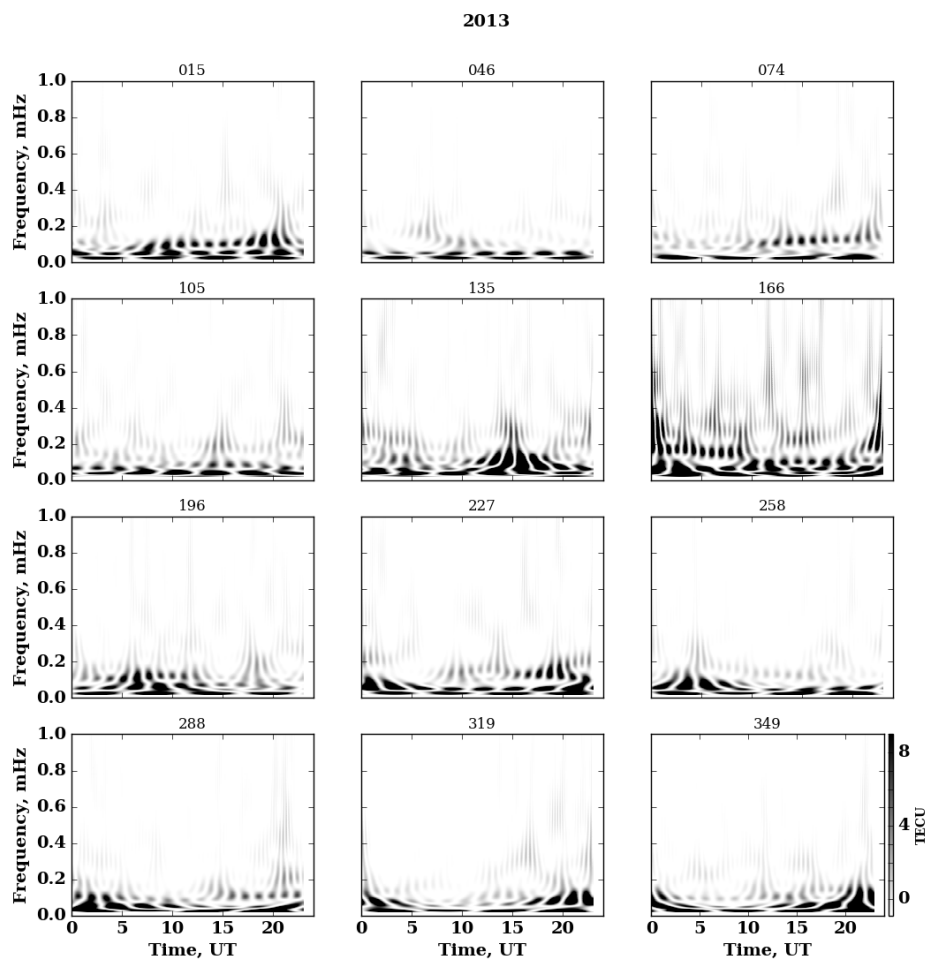


Figure 4.7 - Spectrogram of TEC data derived from receiver at CambridgeBay (CBB) on year 2014. The TEC data on representative days of 12 months are plotted in panels and the number of day is denoted at the top of each panel.

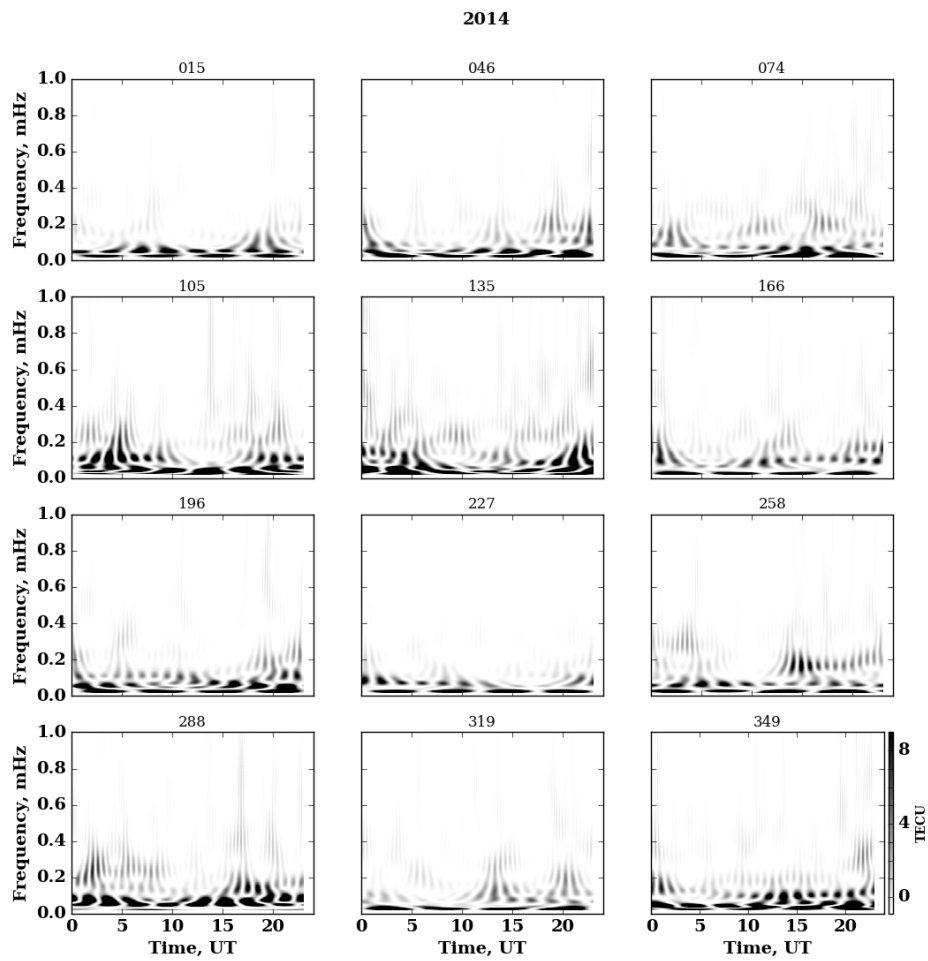


Figure 4.8 - Spectrogram of TEC data derived from receiver at CambridgeBay (CBB) on year 2015. The TEC data on representative days of 12 months are plotted in panels and the number of day is denoted at the top of each panel. The unusual spectrogram on day 288 is not physical and is caused by unavailability of data.

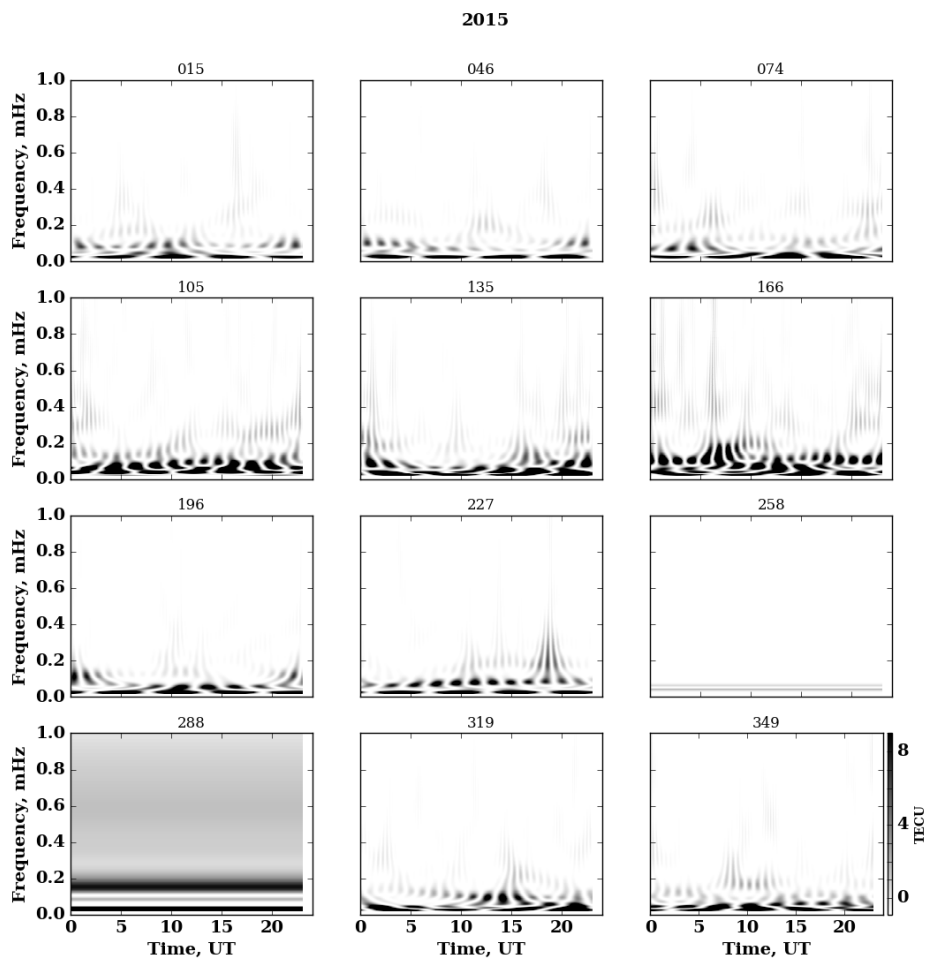
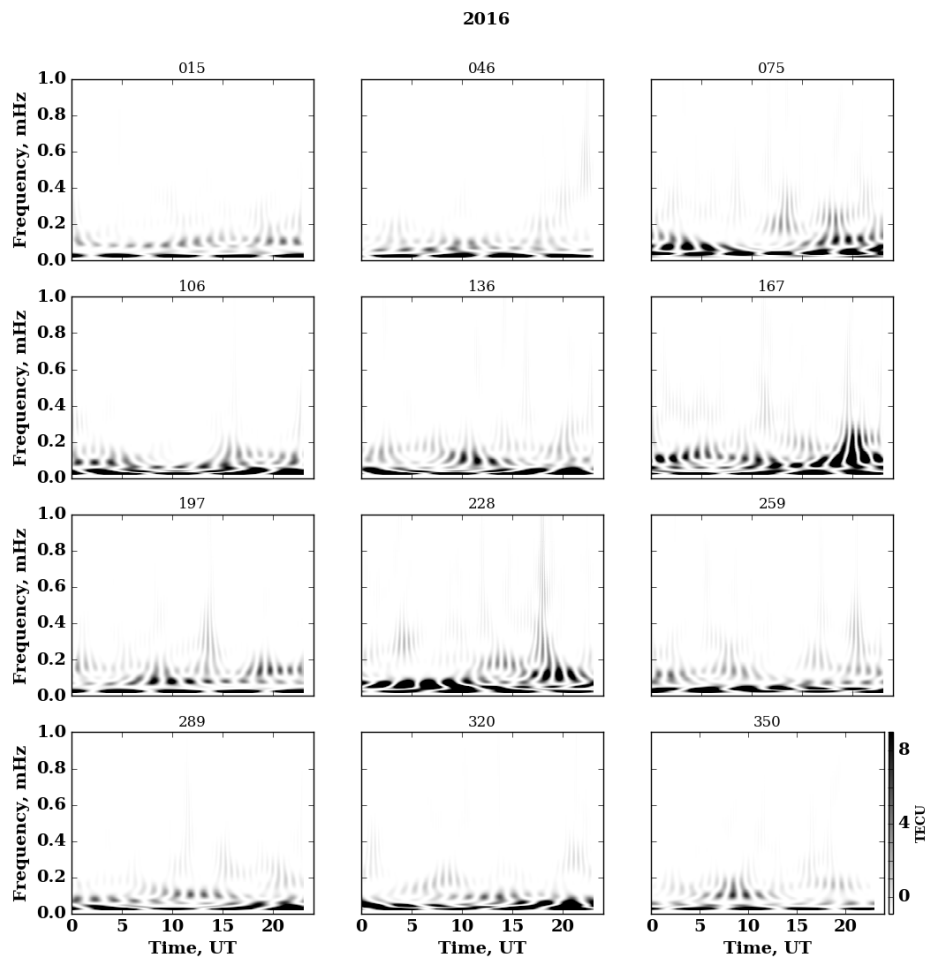


Figure 4.9 - Spectrogram of TEC data derived from receiver at CambridgeBay (CBB) on year 2016. The TEC data on representative days of 12 months are plotted in panels and the number of day is denoted at the top of each panel.



5 POSSIBLE ORIGIN MECHANISMS OF MSTIDS

High latitude MSTIDs are manifestation of Atmosphere-Ionosphere coupling involving Atmospheric waves, namely Acoustic Gravity Waves (RICHMOND, 1978; HUNSUCKER, 1982). The sources that launches these waves, are tropospheric convections, polar vortex, Joule heating associated with the precipitation (KHERANI et al., 2011; WATSON et al., 2016). In the high latitude, the Joule heating is the most preferred source for the MSTIDs. The precipitation can arise from dayside cusp and nightside boundary layers, both of them highly active even during solar quiet-time conditions (PROLSS, 2004). The nightside null or X point also hosts energetic MHD waves known as Pc1-Pc5, that propagate towards high-latitude Ionosphere along the stretched geomagnetic field lines (PROLSS, 2004). Pulsating aurora in the polar ionosphere which has frequency in 1-4 mHz with similar frequency pulsation in ground magnetometer data are manifestation of modulation of the precipitation by Pc5 MHD waves of magnetospheric origin (WEATHERWAX et al., 1997).

5.1 Quiet-time Geomagnetic Disturbances (GMDs) in the polar cap/oval region

Auroral intensification and magnetic disturbances in the high-latitude Ionosphere are signatures of precipitation dynamics. The quiet-time MSTIDs and geomagnetic disturbances (GMDs) of order of 10 nT in the polar oval are simultaneously reported (HUANG et al., 1998; SHIOKAWA et al., 2012). This raise the possibilities that either they have common origin mechanism such as AGWs or the GMDs are indicator of Joule current that heats the E region of Ionosphere that subsequently excites the AGWs and MSTIDs (FRISSELL et al., 2016; SHIOKAWA et al., 2012; WATSON et al., 2016).

In chapter 3, one such connection between MSTIDs and GMDs on day 08 December 2009 was presented. In this chapter, statistics of GMDs will be presented and their possible connection with MSTIDs will be explored.

The GMDs are derived using magnetometer at Cambridge Bay (CBB) of CANadian Magnetic Observatory System (CANMOS) network that provides the three components of magnetic field and total magnetic field with the time resolution of 1 minutes. The same CBB station was selected to investigate the seasonal/solar-flux variabilities of the MSTIDs in the polar cap/oval region, as presented in chapter 4 in

Figures 4.6-4.9. In Figures 5.1-5.4, spectrograms of total magnetic field, are plotted in same format as of Figures 4.6-4.9.

It is noted that the GMDs are present almost on every month though with varying spectral characteristics. Though the maximum value in the gray scale is 0.5 nT but this scale is saturated, in order to capture the weak GMDs. Otherwise, the largest amplitude, represented by dark black, can be in the range of 2-3 nT.

It is noted that the winter and summer GMDs are strongest during high and low solar-flux conditions respectively. This aspect is similar to the variabilities of MSTIDs as noted in Figures 4.6-4.9. Therefore, MSTIDs and GMDs either share common origin mechanism and/or GMDs are indicators of enhanced Joule current associated with the precipitation/Alfven waves dynamics which in turn are responsible for the launching of AGWs and subsequent generation of MSTIDs.

5.2 Numerical Experiments

In order to further probe into these plausible mechanisms, Numerical Experiments (NEs) of AGWs are performed in which Equations (2.2-2.4) are solved numerically, as discussed in section (2.2). The Joule heating associated with the precipitation dynamics in the E region, as described in equations (2.8-2.9) in section 2.2.1, is considered. The numerical simulation code is described in section 2.2.

The Joule heating source is centred at 105 km altitude with Gaussian spread of 20 km. In latitude-longitude, the source is centred at CBB with two values of Gaussian spread which are 5° and 20° . Based on these two values, two NEs are performed and referred as NE1 and NE2, respectively.

The simulation volume covers 0-400 km in altitude, 80° - 40° in latitude, $\varphi_o \pm 80^\circ$ in longitude with $\varphi_o = -105^\circ$ i.e. the longitude of the station CBB. The grid resolutions in altitude, latitude and longitude are 10 km, 2° and 2° , respectively. The Joule heating source has temporal variation of Gaussian form with time width equals to 30 minutes, associating it to the oscillations of Pc5 type.

Figures 5.5-5.6 demonstrate the simulation results of AGWs where snapshots of the amplitude of AGWs are shown at few selected time, as indicated at the top of each panel. These snapshots correspond to the altitude of 250 km.

Both NEs reveal generation and equatorward propagation of AGWs. It is noted that in both NEs, AGWs propagate equatorward upto the latitude of 50° - 60° . In NE1, AGWs are spread longitudinally to 20° around CBB while in NE2, the spread is 40° . These characteristics suggest that the horizontal coverage of AGWs is proportional to the horizontal Gaussian spread of the Joule heating source. It also implies that this source is capable of launching highly dynamic AGWs that propagate long distance in latitude without much attenuation.

At this point, it is important to mention that the NEs performed here simulate AGWs and not Pure Gravity Waves (GWs). The difference between two is that the AGWs are highly dynamical in nature and obvious choice of Atmosphere, in comparison to GWs which are the small wavelength/low period limit of AGWs. In contrast to the slow propagation of GWs of order of 100-200 m/s, AGWs propagate with the acoustic speed of the atmosphere which can be in the range of 300-1500 m/s. In AGWs scenario, such large speed is possible even for long periods (above Brunt-Vaisala period which is of order of 15 minutes in the thermosphere) since these waves are capable of launching long wavelength of order of 100-500 km, unlike the small wavelength of GWs (KHERANI et al., 2011).

In order to have long distance propagation, pure GWs demand ideal conditions such as wind/collision free atmosphere. This make the GWs unfavorable candidate for the long-distance propagating TIDs (RICHMOND, 1978). On the other hand, AGWs do not demand such restrictive conditions and they can propagate unconditionally to long distances, as evident from NE1-NE2 in the present study. This is mainly because they are capable of launching long wavelengths and fast propagating waves. Therefore, the long distance propagating MSTIDs can be interpreted based on AGWs.

Figure 5.1 - Geomagnetic Disturbances (GMDs) observations: Spectrogram of magnetic field data derived from magnetometer at Cambridge Bay (CBB) on year 2013. The magnetic data on representative days of 12 months are plotted in panels and the number of day is denoted at the top of each panel.

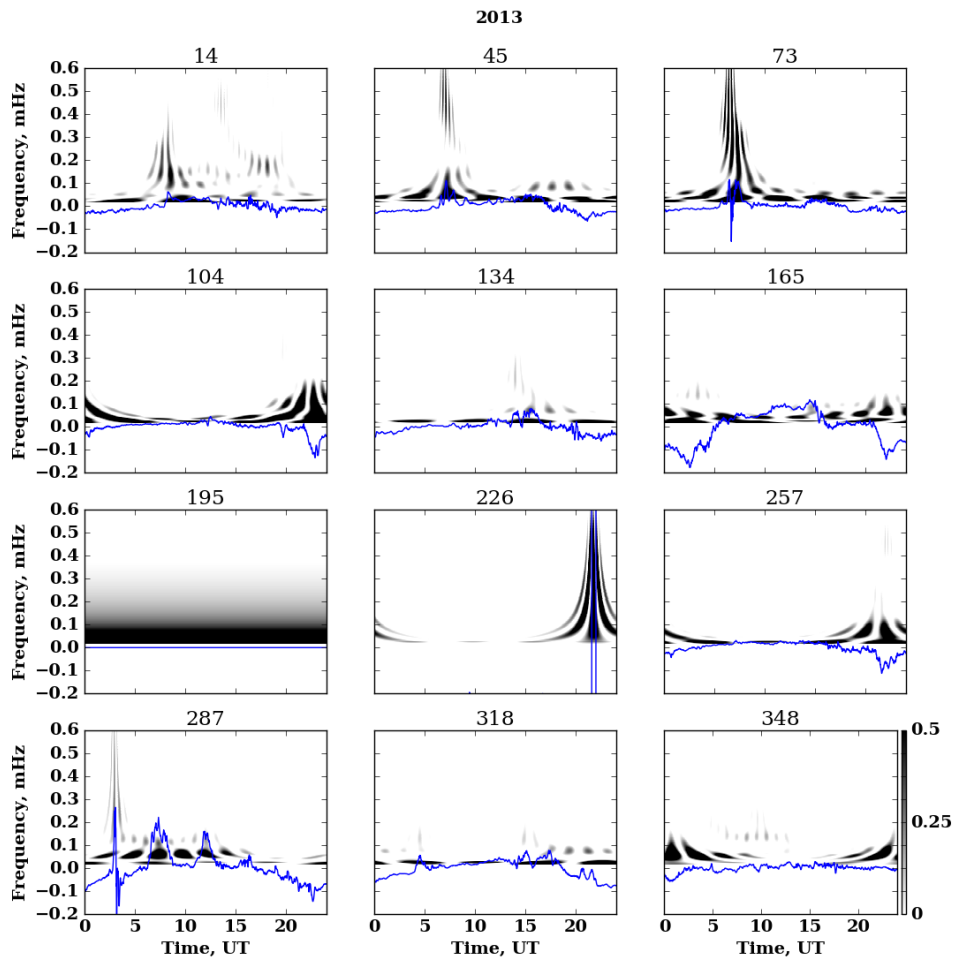


Figure 5.2 - Geomagnetic Disturbances (GMDs) observations: Spectrogram of magnetic field data derived from magnetometer at Cambridge Bay (CBB) on year 2014. The magnetic data on representative days of 12 months are plotted in panels and the number of day is denoted at the top of each panel.

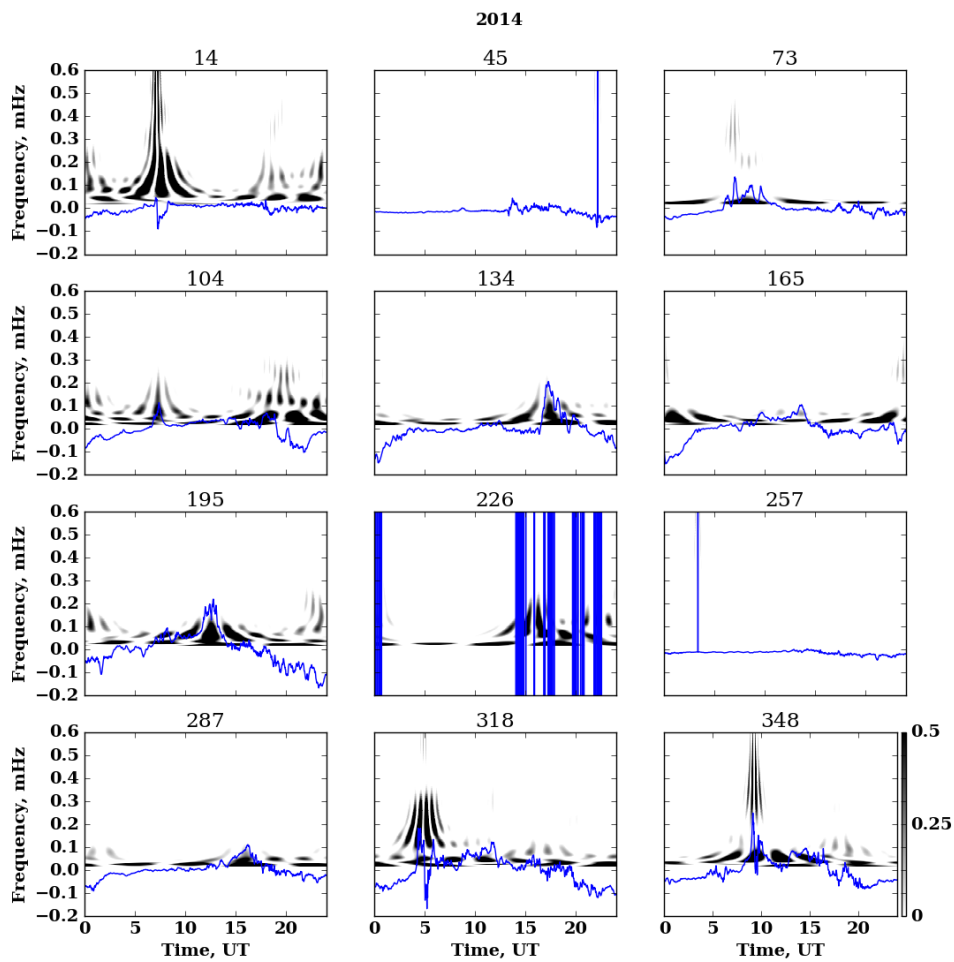


Figure 5.3 - Geomagnetic Disturbances (GMDs) observations: Spectrogram of magnetic field data derived from magnetometer at Cambridge Bay (CBB) on year 2015. The magnetic data on representative days of 12 months are plotted in panels and the number of day is denoted at the top of each panel.

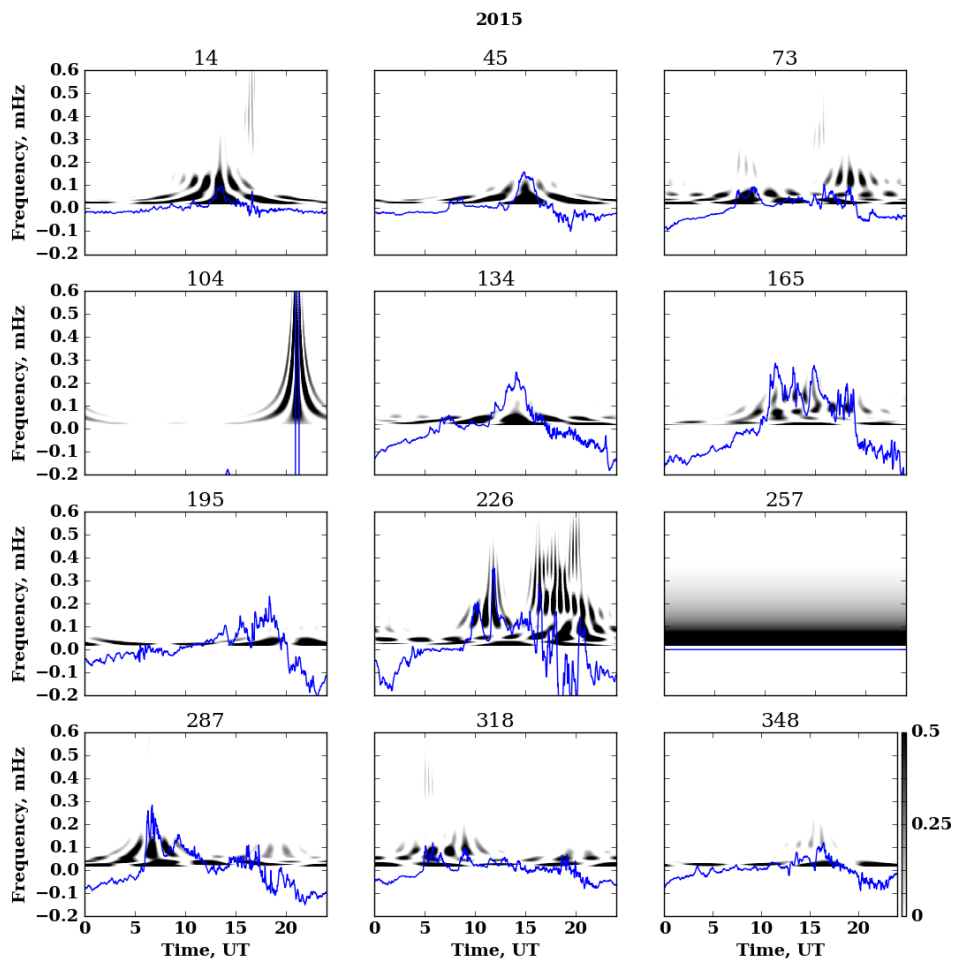


Figure 5.4 - Geomagnetic Disturbances (GMDs) observations: Spectrogram of magnetic field data derived from magnetometer at Cambridge Bay (CBB) on year 2016. The magnetic data on representative days of 12 months are plotted in panels and the number of day is denoted at the top of each panel.

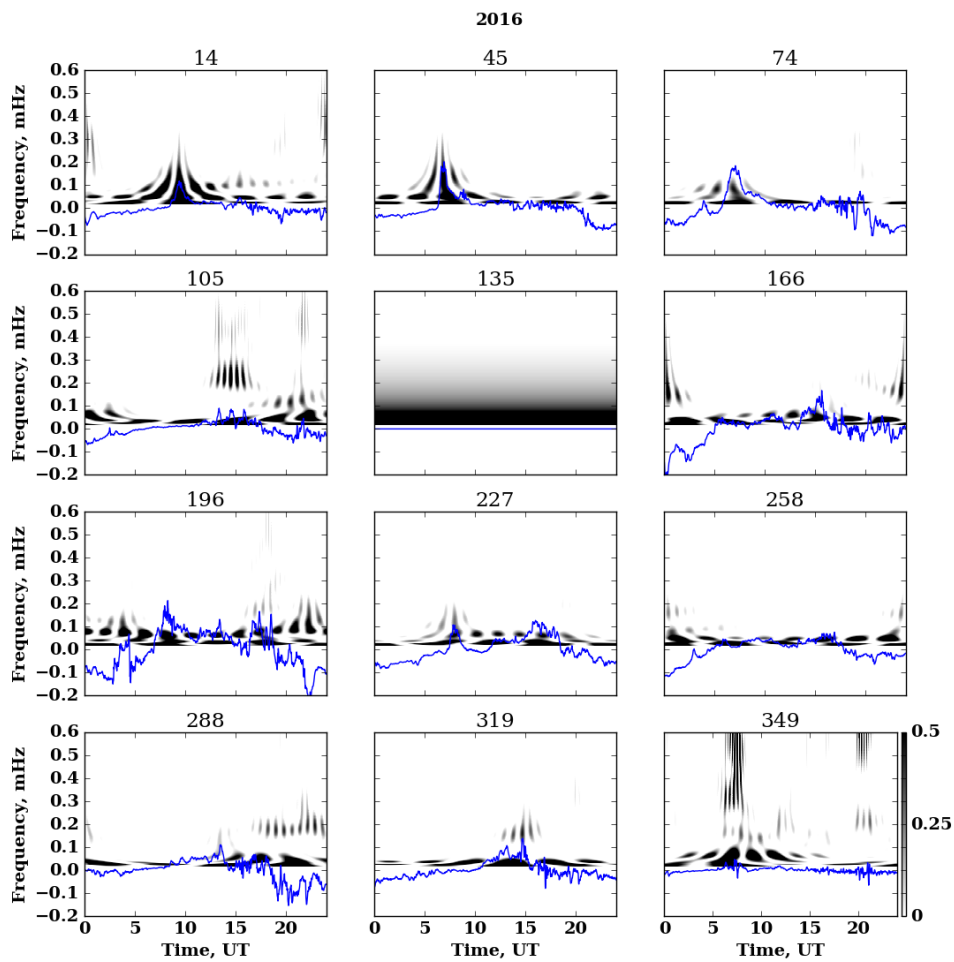


Figure 5.5 - Numerical Experiment of AGWs: The longitudinal wind component of AGWs is shown. Red and blue surfaces correspond to the positive and negative signs of the wind component. The Joule heating is centred at 105 km altitude with Gaussian spread of 20 km. It is centred at latitude-longitude of CBB and has Gaussian spread of 5° in latitude-longitude.

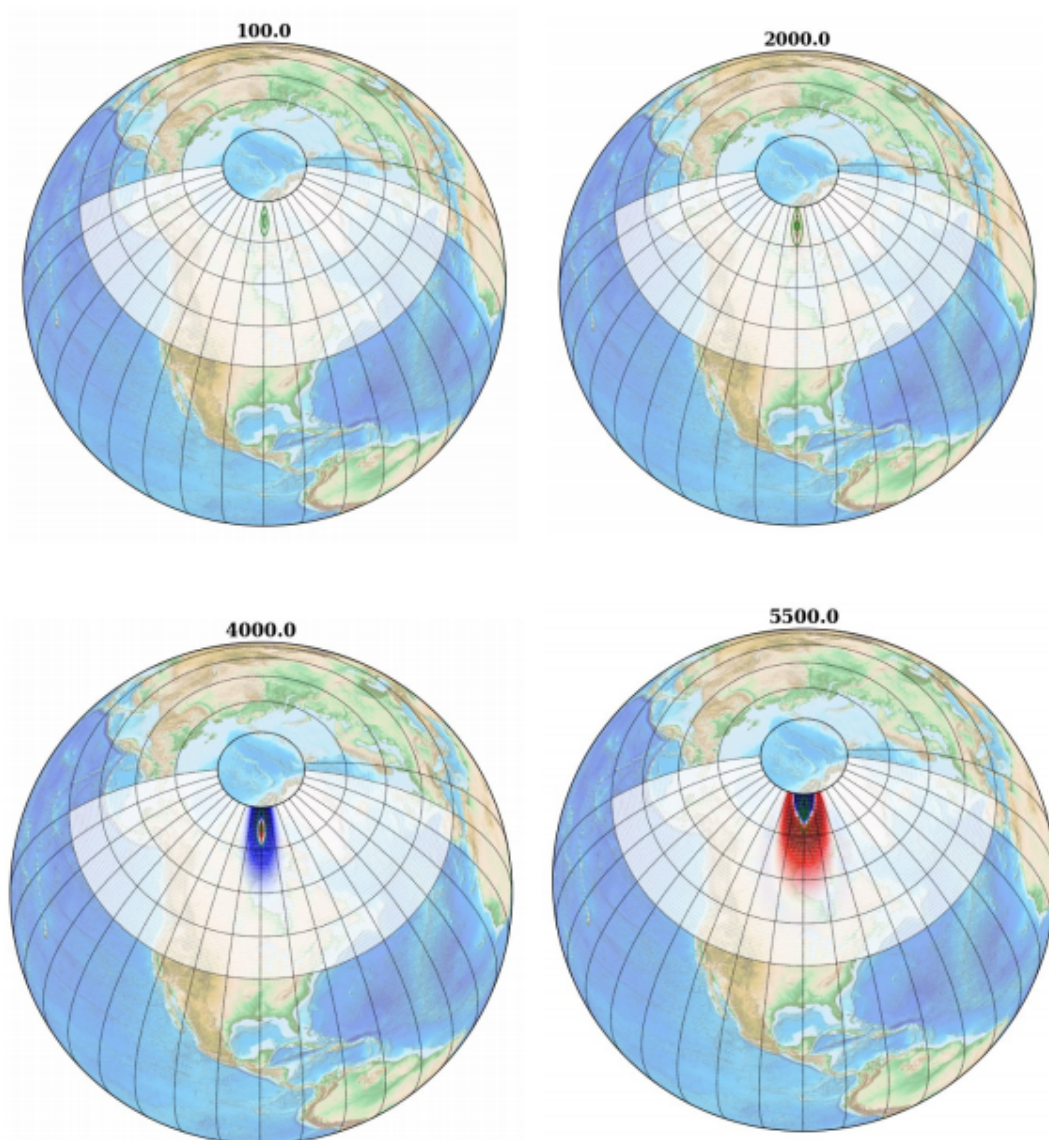
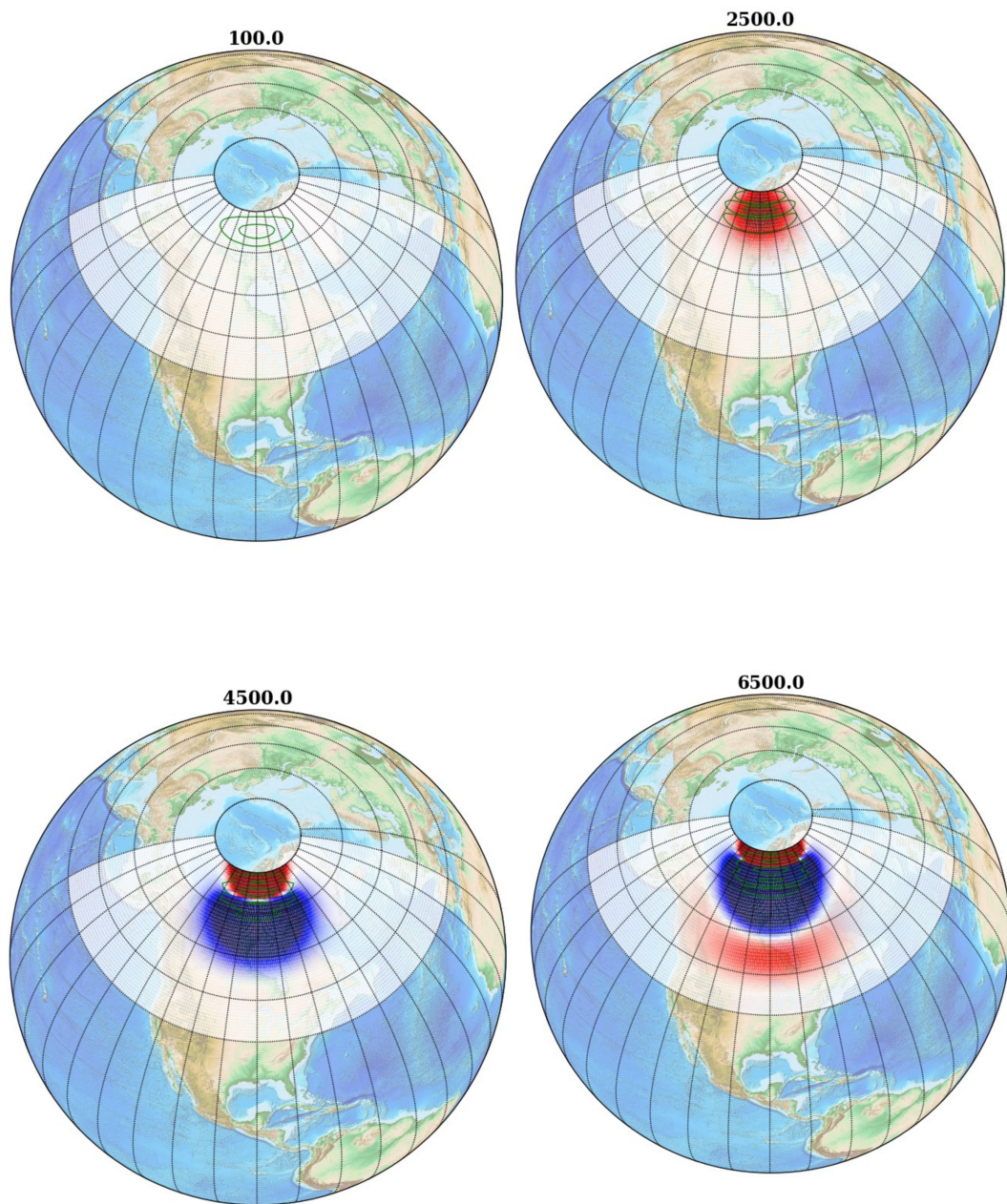


Figure 5.6 - Numerical Experiment of AGWs: The longitudinal wind component of AGWs is shown. Red and blue surfaces correspond to the positive and negative signs of the wind component. The Joule heating is centred at 105 km altitude with Gaussian spread of 20 km. It is centred at latitude-longitude of CBB and has Gaussian spread of 5° in latitude-longitude.



6 CONCLUSIONS

In this doctoral thesis, I have studied the dynamics of high-latitude MSTIDs during quiet-time condition. The study is presented in five chapters. In chapter 1, I presented the objectives of my thesis in section 1.5. In Chapter 2, the data analysis tools to analyse the TEC data from GNSS receivers of CHAIN network are presented. Chapter 3 presents the TEC disturbances on quiet day of 8 December 2009. The study finds dayside MSTIDs which are counterparts of previously reported nightside MSTIDs on the same day. The methodology adopted in this chapter enable to capture MSTIDs and their propagation characteristics. Chapter 4 presents the seasonal and solar-flux variabilities of MSTIDs based on 4 years data covering high solar flux year 2013 to low solar-flux year 2016. In chapter 5, seasonal and solar flux-variabilities of the geomagnetic field, as registered from the ground-based magnetometers of CANMOS (CANadian Magnetometer Observation System) network, are presented. In this chapter, the Numerical Experiments of Acoustic-Gravity Waves are also presented, to understand the origin of MSTIDs from the Joule heating source. The important findings of my thesis are listed as follows:

1. From relatively low dense GNSS network such as CHAIN, various propagation characteristics of the MSTIDs can be obtained if the suitable methodology for the data analysis, as discussed in chapter 2-3, is adopted,
2. This methodology identifies the dayside MSTIDs on 8 of December 2009, the same day when nightside MSTIDs were reported by [Shiokawa et al. \(2012\)](#) over Norway,
3. The spectral characteristics reveal that the MSTIDs reside in 0.2-1 mHz i.e. that have period in the range of 15-80 minutes. The life-time of MSTIDs is about 2 hours and they have 4 periodic surges in a day. These characteristics suggest the involvement of Tides and AGWs in the dynamics of MSTIDs. It also suggest the involvement of Pc5 MHD waves of boundary layer origin,
4. The constructed keograms reveal the presence of both poleward/equatorward propagating MSTIDs, with velocity in the range of 250-500 m/s,
5. They propagate long distance of about 30° in latitude and disturb the mid-latitude Ionosphere,
6. The MSTIDs are stronger in winter month of high solar-flux year and summer month of low solar-flux year. This suggests their association with the solar driven dynamics, namely the Joule heating from the precipitation dynamics,

7. The similar variabilities and spectral characteristics are found in the Geomagnetic Disturbances (GMDs) in the magnetic field data, registered from the magnetometer at polar oval station CBB. These similarities suggest that both MSTIDs and GMDs either share common origin mechanism and/or GMDs are indicators of enhanced Joule current associated with the precipitation/MHD waves dynamics which in turn are responsible for the launching of AGWs and subsequent generation of MSTIDs.
8. The Numerical Experiment confirms the generation of AGWs from the Joule heating source,
9. The simulated AGWs are found to propagate long distance similar to the observed MSTIDs. This implies that the AGWs, rather than pure GWs, are responsible for the MSTIDs since GWs can not propagate such long distance, as shown by [Richmond \(1978\)](#).

REFERENCES

- BARROS, D.; TAKAHASHI, H.; WRASSE, C. M.; FIGUEIREDO, C. A. O. B. Characteristics of equatorial plasma bubbles observed by tec map based on ground-based gnss receivers over south america. **Annales Geophysicae**, v. 36, n. 1, p. 91–100, 2018. 13
- FRANCIS, S. H. A theory of medium-scale traveling ionospheric disturbances. **Journal of Geophysical Research**, v. 79, n. 34, p. 5245–5260, 1974. 19
- FRISSELL, N. A.; BAKER, J. B. H.; RUOHONIEMI, J. M.; GREENWALD, R. A.; GERRARD, A. J.; MILLER, E. S.; WEST, M. L. Sources and characteristics of medium-scale traveling ionospheric disturbances observed by high-frequency radars in the north american sector. **Journal of Geophysical Research: Space Physics**, v. 121, n. 4, p. 3722–3739, 2016. 7, 8, 21, 22, 43
- HALL, G. E.; MACDOUGALL, J. W.; CECILE, J.-F.; MOORCROFT, D. R.; ST.-MAURICE, J. P. Finding gravity wave source positions using the super dual auroral radar network. **Journal of Geophysical Research: Space Physics**, v. 104, n. A1, p. 67–78, 1999. 8
- HARGREAVES, J. K. **The solar-terrestrial environment**. Cambridge: Cambridge University Press, 1992. 7
- HERNÁNDEZ-PAJARES, M.; JUAN, J. M.; SANZ, J.; ARAGÓN-ÀNGEL, A. Propagation of medium scale traveling ionospheric disturbances at different latitudes and solar cycle conditions. **Radio Science**, v. 47, n. 6, p. RS0K05, 2012. 29, 31, 32
- HINES, C. O. **The solar-terrestrial environment**. Washington: American Geophysical Union, 1974. 7
- HUANG, C.-S.; DIETER, A. A.; SOFKO, G. J. High-latitude ionospheric perturbations and gravity waves: 1. observational results. **Journal of Geophysical Research**, v. 103, n. A2, p. 2131–2142, 1998. 7, 43
- HUNSUCKER, R. D. Atmospheric gravity waves generated in the high-latitude ionosphere: a review. **Reviews of Geophysics**, v. 20, n. 2, p. 293–315, 1982. 43
- HUNSUCKER, R. D.; HARGREAVES, J. K. **The high latitude Ionosphere and its effects on radio propagation**. Cambridge: Cambridge University Press, 2003. 5, 7

ISHIDA, T.; HOSOKAWA, K.; SHIBATA, T.; SUZUKI, S.; NISHITANI, N.; T., O. Superdarn observations of daytime mstids in the auroral and mid-latitudes: Possibility of long-distance propagation. **Geophysical Research Letters**, v. 35, n. 13, p. L13102, 2008. [8](#), [32](#)

JAYACHANDRAN, P. T.; HOSOKAWA, K.; MACDOUGALL, J. W.; MUSHINI, S.; LANGLEY, R. B.; SHIOKAWA, K. Gps total electron content variations associated with a polar cap arc. **Journal of Geophysical Research: Space Physics**, v. 114, n. A12, p. A12304, 2009a. [11](#), [30](#)

JAYACHANDRAN, P. T.; LANGLEY, R. B.; MACDOUGALL, J. W.; MUSHINI, S. C.; POKHOTELOV, D.; HAMZA, A. M.; MANN, I. R.; MILLING, D. K.; KALE, Z. C.; CHADWICK, R.; KELLY, T.; DANSKIN, D. W.; CARRANO, C. S. Canadian high arctic ionospheric network (chain). **Geophysical Research Letters**, v. 44, n. 1, p. 1–10, 2009b. [6](#), [11](#)

JONAH, O. F.; KHERANI, E. A.; PAULA, E. R. D. Observation of tec perturbation associated with medium-scale traveling ionospheric disturbance and possible seeding mechanism of atmospheric gravity wave at a brazilian sector. **Journal of Geophysical Research: Space Physics**, v. 121, n. 3, p. 2531–2546, 2016. [8](#)

KELLEY, M. C. **The Earth's ionosphere, plasma physics and electrodynamics**. San Diego: Elsevier, 2009. [1](#), [3](#)

KHERANI, E.; ABDU, M.; FRITTS, D.; PAULA, E. de. The acoustic gravity wave induced disturbances in the equatorial ionosphere. In: ABDU, M. A.; PANCHEVA, D. (Ed.). **Aeronomy of the Earth's atmosphere and ionosphere**. Dordrecht: Springer, 2011. v. 2, p. 141–162. [43](#), [45](#)

KHERANI, E.; ROLLAND, L.; LOGNONNÉ, P.; SLADEN, A.; KLAUSNER, V.; PAULA, E. de. Traveling ionospheric disturbances propagating ahead of the tohoku-oki tsunami: a case study. **Geophysical Journal International**, v. 204, n. 2, p. 1148–1158, 2016. [14](#)

MACDOUGALL, J. W.; ANDRE, D. A.; SOFKO, G. J.; HUANG, C.-S.; KOUSTOV, A. V. Travelling ionospheric disturbance properties deduced from super dual auroral radar measurements. **Annales Geophysicae**, v. 18, n. 12, p. 1550–1559, 2000. [8](#)

MAKAREVICH, R. A.; NICOLLS, M. J. Statistical comparison of tec derived from gps and isr observations at high latitudes. **Radio Science**, v. 48, n. 4, p. 441–452, 2013. 8

MOSERT, M.; MCKINNELL, L.-A.; GENDE, M.; BRUNINI, C.; ARAUJO, J.; EZQUER, R.; CABRERA, M. Variations of fof2 and gps total electron content over the antarctic sector. **Earth, Planets and Space**, v. 63, n. 4, p. 327–333, 2011. 8

OINATS, A.; NISHITANI, N.; PONOMARENKO, P.; BERNGARDT, O.; RATOVSKEY, K. Statistical characteristics of medium-scale traveling ionospheric disturbances revealed from the hokkaido east and ekaterinburg hf radar data. **Earth Planets and Space**, v. 68, n. 1, p. 8, 2016. 8

OTSUKA, Y.; SUZUKI, K.; NAKAGAWA, S.; NISHIOKA, M.; SHIOKAWA, K.; TSUGAWA, T. Gps observations of medium-scale traveling ionospheric disturbances over europe. **Annales Geophysicae**, v. 31, n. 2, p. 163–172, 2013. 7, 9

PAULINO, I. **Estudo da propagação de ondas de gravidade na termosfera-ionosfera**. 2012. 274 p. (02.07.16.25-TDI). Tese (Doutorado em Geofísica Espacial/Ciências Atmosféricas) — Instituto Nacional de Pesquisas Espaciais (INPE), São José dos Campos, 2012. Available from: <<http://urlib.net/8JMKD3MGP7W/3BB4LPS>>. Access in: 2018. 13, 14

PROLSS, G. W. **Physics of the Earth's space environment**. Berlin: Springer-Verlag Berlin Heidelberg, 2004. 159-272. 1, 2, 6, 16, 17, 43

RICHMOND, A. D. Gravity wave generation, propagation, and dissipation in the thermosphere. **Journal of Geophysical Research: Space Physics**, v. 83, n. A9, p. 4131–4145, 1978. 22, 32, 43, 45, 54

SHIOKAWA, K.; MORI, M.; OTSUKA, Y.; OYAMA, S.; NOZAWA, S. Motion of high-latitude nighttime medium-scale traveling ionospheric disturbances associated with auroral brightening. **Journal of Geophysical Research: Space Physics**, v. 117, n. A10, p. 485–488, 2012. 7, 8, 10, 11, 19, 20, 21, 22, 23, 43, 53

SOFKO, G.; HUANG, C.-S. Superdarn observations of medium-scale gravity wave pairs generated by joule heating in the auroral zone. **Geophysical Research Letters**, v. 27, n. 4, p. 485–488, 2000. 7

SWENSON, G. R.; LIU, A. Z.; LI, F.; TANG, J. High frequency atmospheric gravity wave damping in the mesosphere. **Advances in Space Research**, v. 32, n. 5, p. 785–793, 2003. 13

TAKAHASHI, H.; TAYLOR, M. J.; PAUTET, P.-D.; MEDEIROS, A. F.; GOBBI, D.; WRASSE, C. M.; FECHINE, J.; ABDU, M. A.; BATISTA, I. S.; PAULA, E.; SOBRAL, J. H. A.; ARRUDA, D.; VADAS, S. L.; SABBAS, F. S.; FRITTS, D. C. Simultaneous observation of ionospheric plasma bubbles and mesospheric gravity waves during the spreadfex campaign. **Annales Geophysicae**, v. 27, n. 4, p. 1477–1487, 2009. 13

TAYLOR, M. J.; PAUTET, P.-D.; MEDEIROS, A. F.; BURITI, R.; FECHINE, J.; FRITTS, D. C.; VADAS, S. L.; TAKAHASHI, H.; SABBAS, F. T. São. Characteristics of mesospheric gravity waves near the magnetic equator, Brazil, during the spreadfex campaign. **Annales Geophysicae**, v. 27, n. 2, p. 461–472, 2009. 13

WATSON, C.; JAYACHANDRAN, P. T.; MACDOUGALL, J. W. Characteristics of GPS TEC variations in the polar cap ionosphere. **Journal of Geophysical Research: Space Physics**, v. 121, n. 5, p. 4748–4768, 2016. 7, 11, 19, 21, 22, 29, 32, 43

WATSON, C.; JAYACHANDRAN, P. T.; SPANSWICK, E.; DONOVAN, E. F.; DANSKIN, D. W. GPS TEC technique for observation of the evolution of substorm particle precipitation. **Journal of Geophysical Research: Space Physics**, v. 116, n. A10, p. A00I90, 2011. 21

WEATHERWAX, A.; ROSENBERG, T.; MAXLENNAN, C.; DOOLITTLE, J. Substorm precipitation in the polar cap and associated Pc5 modulation. **Geophysical Research Letters**, v. 24, n. 5, p. 579–582, 1997. 6, 30, 43